



Cancer-Associated Fibroblasts Foster a High-Lactate Microenvironment to Drive Perineural Invasion in Pancreatic Cancer

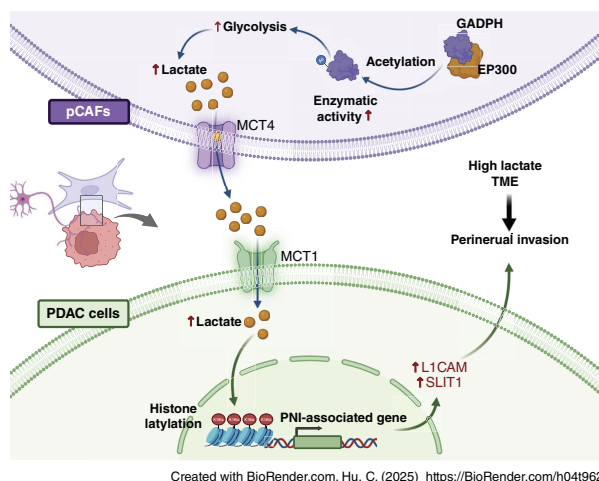
Tingting Li^{1,2,3,4}, Chonghui Hu^{1,2}, Tianhao Huang^{1,2,4}, Yu Zhou^{1,2}, Qing Tian^{3,4}, Huimou Chen⁵, Rihua He^{1,2,4}, Yuan Yuan⁶, Yong Jiang^{1,2,4}, Honghui Jiang^{1,2,4}, Kaijun Huang², Di Cheng⁵, Rufu Chen^{1,2,3,6}, and Shangyou Zheng^{1,2}

ABSTRACT

Perineural invasion (PNI) is a pivotal prognostic factor in pancreatic cancer, associated with aggressive tumor behavior and adverse patient outcomes. The recognized clinical impact of PNI highlights the need to better understand the molecular mechanisms underlying PNI-induced phenotypes. In this study, we isolated PNI-associated cancer-associated fibroblasts (pCAF), which demonstrated a markedly enhanced capacity to promote neural invasion in pancreatic cancer compared with non-PNI-associated CAFs. Single-cell, high-throughput sequencing and metabolomics data showed a significant upregulation of glycolysis in pCAFs, fostering a high-lactate tumor microenvironment conducive to cancer progression. pCAF-derived lactate was absorbed by tumor cells, facilitating histone H3K18 lactylation. The lactate-induced epigenetic modification activated the transcription of neural invasion-associated genes, such as *LICAM* and *SLIT1*, thereby driving PNI in pancreatic cancer. Further exploration of metabolic reprogramming in pCAFs revealed enhanced acetylation of the glycolytic enzyme GAPDH, which correlated with increased enzymatic activity and glycolytic flux. Targeting GAPDH and lactylation modifications significantly inhibited neural invasion in a genetically engineered mouse model. Clinical data suggested that high levels of H3K18 lactylation correlate with severe PNI and poorer patient prognosis. Together, these findings provide critical insights into the role of CAFs in promoting PNI of pancreatic cancer, highlighting glycolytic reprogramming and lactate-

driven histone modifications as potential therapeutic targets for PDAC.

Significance: Targeting cancer-associated fibroblast metabolism or histone lactylation in pancreatic cancer cells to reverse epigenetic remodeling induced by lactate accumulation in the tumor microenvironment are potential therapeutic strategies to inhibit perineural invasion.



Introduction

Perineural invasion (PNI) is a significant biological characteristic of pancreatic cancer, manifested by the infiltration of tumor cells into neural tissues, facilitating their spread and metastasis (1). PNI is closely associated with early disease progression and postoperative

recurrence and is recognized as an independent factor for poor prognosis in patients. Pancreatic ductal adenocarcinomas (PDAC) have a high incidence of PNI, affecting 80% to 100% of cases (2), with neural remodeling occurring even at the early intraepithelial neoplastic stage (3, 4). Our previous randomized controlled trial

¹Department of Pancreas Center, Guangdong Provincial People's Hospital (Guangdong Academy of Medical Sciences), Southern Medical University, Guangzhou, China. ²Department of General Surgery, Guangdong Provincial People's Hospital (Guangdong Academy of Medical Sciences), Southern Medical University, Guangzhou, China. ³School of Medicine, South China University of Technology, Guangzhou, China. ⁴Guangdong Provincial People's Hospital (Guangdong Academy of Medical Sciences), Southern Medical University, Guangzhou, China. ⁵Department of Oncology, Sun Yat-sen Memorial Hospital of Sun Yat-sen University, Guangzhou, China. ⁶Guangdong Cardiovascular Institute, Guangdong Provincial People's Hospital, Guangdong Academy of Medical Sciences, Guangzhou, China.

T. Li, C. Hu, T. Huang, and Y. Zhou contributed equally to this article.

Corresponding Authors: Di Cheng, Sun Yat-sen Memorial Hospital of Sun Yat-sen University, 107 Yan Jiang West Road, Yuexiu District, Guangzhou 510120, Guangdong, China. E-mail: chengdi@mail.sysu.edu.cn; Rufu Chen, Guangdong Provincial People's Hospital (Guangdong Academy of Medical Sciences), No. 106 Zhongshan Second Road, Yuexiu District, Guangzhou 510080, Guangdong, China. E-mail: chenrufu@gdph.org.cn; and Shangyou Zheng, zhengshangyou@gdph.org.cn

Cancer Res 2025;85:2199–2173

doi: 10.1158/0008-5472.CAN-24-3173

This open access article is distributed under the Creative Commons Attribution-NonCommercial-NoDerivatives 4.0 International (CC BY-NC-ND 4.0) license.

©2025 The Authors; Published by the American Association for Cancer Research

demonstrated that standard Whipple surgery combined with modified retroperitoneal nerve dissection significantly improved disease-free survival (DFS) in patients with pancreatic head cancer. Additionally, the procedure significantly alleviated postoperative back pain, highlighting the critical importance of targeting PNI in pancreatic cancer (5). The concurrent occurrence of tumor microenvironment (TME) remodeling and PNI during the intraepithelial neoplastic stage suggests a close relationship between these two phenomena, underscoring the need for further research in this area (6).

The TME, with its complex network of cells, signaling molecules, and extracellular matrix components, plays a crucial role in PNI of pancreatic cancer through its interactions with cancer cells (7). Previous research has found that leukemia inhibitory factor (LIF) secreted by stromal cells in the PDAC microenvironment induces nerve cell migration and differentiation, which is positively correlated with neural remodeling and axonogenesis (8). Our recent study identified that cancer-associated fibroblasts (CAF) promote PNI in pancreatic cancer by delivering noncoding RNA PNI-associated transcript (*PIAT*) to cancer cells via extracellular vesicles, regulating *YBX1*-dependent m5C modification (9). Banh and colleagues (10) highlighted that metabolic remodeling of the TME, particularly the release of serine by peripheral axons, is crucial for supporting PDAC growth and promoting neural invasion under nutrient-poor conditions. Auciello and colleagues (11) revealed that pancreatic stellate cell-derived lysophosphatidylcholines and the autotaxin-lysophosphatidic acid axis significantly promote PDAC progression by enhancing cancer cell proliferation and migration. However, the metabolic contribution of CAFs in the process of PNI in pancreatic cancer has not been explored.

Lactate metabolism is a crucial biological process following the activation of glycolysis. The remodeling of the tumor lactate metabolic microenvironment promotes tumor progression and metastasis by regulating autophagy, mitochondrial activity, immune evasion, and epigenetic modifications in tumor cells (12, 13). The glycolysis-activated high-lactate microenvironment created by CAFs mediates lipid droplet deposition and histone acetylation of the lipoprotein PLIN2 in prostate cancer cells, thereby promoting tumor metastasis (14). Certain metabolites play dual roles: They are not only essential for energy production and biomass formation but also crucial in modulating gene and protein expression, thereby affecting the behavior of cancer cells within the TME (15). Histone lactylation, a key mechanism of the high-lactate microenvironment, is increasingly being revealed to play a crucial role in regulating tumor metabolic reprogramming, invasion and metastasis, drug resistance, and immune evasion (16–18). In PDAC, Wang and colleagues (19) revealed the regulatory role of histone lactylation in tumor metastasis, offering novel insights into its potential for prognostic prediction, patient stratification, and therapeutic targeting within the metabolism–epigenetics–immunity axis. However, the mechanisms by which CAFs remodel the lactate metabolic microenvironment in pancreatic cancer and subsequently regulate PNI through histone lactylation are yet to be elucidated.

In this study, we aimed to elucidate the mechanisms by which CAFs support PNI in PDAC. Using both *in vivo* and *in vitro* models, we found that CAFs derived from patients with PDAC with positive PNI (PNI⁺) significantly enhance tumor cell invasion toward nerves. Mechanistically, we discovered that PNI⁺ CAFs exhibit increased acetylation levels of the glycolytic enzyme GAPDH, enhancing its enzymatic activity and thereby boosting glycolysis and lactate secretion. This leads to elevated lactylation levels of histone H3K18 on

tumor cells, which in turn transcriptionally activates *LICAM* and *SLIT1*, ultimately promoting PNI. Our study underscores the pivotal role of CAF-derived lactate in the TME through the lactylation of H3K18 in promoting PNI and proposes a novel therapeutic strategy targeting this lactate metabolism or H3K18 lactylation (H3K18la) to suppress PNI in pancreatic cancer.

Materials and Methods

Patients and specimens

From December 2014 to October 2023, tumor tissues were collected from 152 patients diagnosed with PDAC following tumor resection at Guangdong Provincial People's Hospital and Sun Yat-sen Memorial Hospital. Patients were eligible for inclusion if they had a confirmed diagnosis of PDAC and had not received radiotherapy or chemotherapy prior to surgery. Exclusion criteria included any history of prior cancer treatments. Patients who were lost to follow-up were excluded. The patient cohort included both male and female subjects, with a sex distribution that did not affect the inclusion of clinical samples. PNI was characterized by the presence of cancer cells encasing at least 33% of the nerve circumference or infiltrating the nerve sheath's epineural, perineurial, or endoneurial compartments. The extent of PNI was evaluated by combining two parameters: the degree of nerve involvement and its frequency. The extent of PNI was scored as 0 (no involvement), 1 (perineural, cancer cells encasing at least 33% of the nerve), or 2 (intraneural, cancer cells infiltrating the nerve sheath compartments). The frequency of PNI was graded as 0 (absent), 1 (low), 2 (moderate), or 3 (high). A composite severity score, obtained by multiplying the extent and frequency scores, ranged from 0 to 6. Patients with scores of 4 to 6 were classified as having severe PNI (PNI⁺), whereas those with scores of 0 to 3 were categorized as PNI-negative (PNI⁻). Written informed consent was obtained from all participants, and the study protocol was approved by the Ethics Committees of Guangdong Provincial People's Hospital and Sun Yat-sen Memorial Hospital.

Multiplex immunofluorescence

Multiplex immunofluorescence (mIF) staining was carried out using the PANO 4-plex IHC Kit (Panovue) according to the manufacturer's instructions. Briefly, tissue sections were deparaffinized, rehydrated, and subjected to antigen retrieval using EDTA buffer (pH 9.0). After blocking with goat serum (Golden Bridge Biotechnology) for 15 minutes, the sections were incubated for 1 hour with the primary antibodies PDPN (26981, Cell Signaling Technology), α SMA (D4K9N, Cell Signaling Technology), Tuj1 (ab52623, Abcam), CK19 (D4G2, Cell Signaling Technology), anti-lactylated lysine rabbit monoclonal antibody (pdm-1401rm, PTM), anti-lactylated histone H3 (Lys18) rabbit monoclonal antibody (ptm-1406rm, PTM), *LICAM* (ab208155, Abcam), or *SLIT1* (ab307436, ab151724, Abcam). After washing three times with Tris-buffered saline with Tween 20 (TBST), the sections were incubated with horseradish peroxidase-conjugated secondary antibodies for 30 minutes, followed by incubation with fluorescent tyramide for 15 minutes. Nuclei were counterstained with DAPI. Images were acquired using a ZEISS LSM 900 confocal microscope (Carl Zeiss Microscopy). ImageJ was used for fluorescence quantification. "High" was defined as net fluorescence intensity >80, and "low" was defined as net fluorescence intensity \leq 80.

Fibroblast isolation and cell culture

CAFs were extracted from PDAC tissues following a modified protocol derived from established methods. Briefly, tissue samples were minced and digested with collagenase at 37°C for 30 minutes, followed by filtration and centrifugation. The cell pellet was resuspended in fibroblast medium (cat. #2301, ScienCell) and cultured. Fibroblasts were collected starting from the second passage, identified based on their morphologic characteristics, and confirmed by immunofluorescence (IF) staining for CAF markers. Primary fibroblasts from passages 2 to 10 were used for experiments. The PDAC cell lines (PANC1 and MiaPaCa-2) were purchased from the ATCC. Primary dorsal root ganglion (DRG) cells were isolated from neonatal Sprague-Dawley rats. The PDAC cell lines (PANC1 and MiaPaCa-2) were cultured in DMEM high glucose (Gibco) supplemented with 10% FBS (Gibco) and 1% penicillin-streptomycin (Sigma) at 37°C in 5% CO₂. Primary DRG cells were cultured in Neurobasal medium (cat. #21103049, Thermo Fisher Scientific).

Gene enrichment analysis

Gene enrichment analyses were performed using the online tools DAVID (<https://david.ncifcrf.gov/>) and the GSEA Java package (version 4.3.3). The Gene Ontology (GO) term, Kyoto Encyclopedia of Genes and Genomes (KEGG) pathway, and Molecular Signatures Database hallmarks with a *P* value < 0.05 or the top 10 GO terms were analyzed.

Enzyme activity assays

Enzyme activities were measured using commercial assay kits, following the protocols provided by the manufacturers. The kits used were the Pyruvate Kinase Activity Assay Kit (ab83432, Abcam), Hexokinase Activity Assay Kit (ab136957, Abcam), Phosphofructokinase Activity Assay Kit (ab155898, Abcam), and Glyceraldehyde-3-Phosphate Dehydrogenase Activity Assay Kit (ab204732, Abcam).

Immunoprecipitation

Cells were lysed on ice for 30 minutes using immunoprecipitation lysis buffer, with gentle agitation every 10 minutes. The lysates were centrifuged at 13,000 rpm for 20 minutes, and the supernatant was collected. The supernatant was then incubated with the specified antibody or IgG control at 4°C overnight with rotation. The following day, protein A/G beads (Thermo Fisher Scientific) were added to the mixture and incubated at room temperature for 1 hour. The precipitated proteins were collected and used for subsequent experimental analyses.

Aerobic glycolysis analysis

Lactate levels in cell culture supernatants and tissue samples were measured using the Lactate Assay Kit (ab65330, Abcam). For cell samples, 500,000 cells were seeded in 6 cm dishes. After 24 hours of adhesion, the medium was replaced with 2 mL of serum-free high-glucose DMEM, and the cells were incubated for 3 hours. Then, 200 µL of supernatant was collected for analysis. For tissue samples, 20 mg of each tissue was homogenized on ice using a Dounce homogenizer in 4 to 6 volumes of lactate assay buffer. The homogenate was centrifuged, and the supernatant was collected. To remove proteins, the supernatant was passed through a 10 kDa ultrafiltration tube at 14,000 g for 15 minutes. Finally, 5 µL of the filtrate was used for lactate measurement. Absorbance was measured at 570 nm using a microplate reader.

Glucose uptake was assessed using the Glucose Uptake Assay Kit (ab136955, Abcam). Cells were seeded in six-well plates at a density of 200,000 cells per well. Once the cells reached 90% confluence, they were cultured in serum-free, low-glucose medium for 12 hours. Cells were then washed three times with PBS and incubated in Krebs-Ringer phosphate buffer for 40 minutes. Cells were stimulated with or without insulin, followed by treatment with 10 mmol/L 2-deoxy-D-glucose (2DG) for 20 minutes. After washing the cells three times with PBS, they were lysed with extraction buffer, and endogenous NAD was removed. The reaction mixture was prepared, and the absorbance at 412 nm was measured in kinetic mode on a microplate reader, with readings taken every 2 to 3 minutes.

Extracellular acidification rate (ECAR) and oxygen consumption rate were measured using the Seahorse XFe96 Analyzer (Agilent) according to the manufacturer's instructions. Cells were seeded at a density of 4,000 cells per well in an XFe96 cell culture plate and incubated for 24 hours. The cells were gently washed and incubated in the base medium (Agilent) for 1 hour before baseline measurements were taken. Various compounds were sequentially injected into each well, and ECAR or oxygen consumption rate was measured accordingly. Data were exported using Seahorse Wave software (Agilent) and analyzed using GraphPad Prism.

Western blot analysis

Cells were lysed on ice for 30 minutes using RIPA lysis buffer, followed by centrifugation at 12,000 rpm for 15 minutes at 4°C to collect the supernatant, which was then quantified using a bicinchoninic acid (BCA) assay kit. The cell lysates were separated by SDS-PAGE, and the proteins were transferred to polyvinylidene difluoride membranes (Millipore). After blocking, the membranes were incubated with primary antibodies overnight at 4°C. The following day, the membranes were washed three times with TBST and incubated with secondary antibodies at room temperature for 1 hour. Immunoreactive bands were visualized using the Chemi XT4 imaging system. Details of the antibodies used are listed in Supplementary Table S1.

qRT-PCR analysis

Total RNA was extracted from cell lines or tissues using a commercial kit (EZB-RN4, EZBioscience). Reverse transcription was performed using the PrimeScript RT Reagent Kit (Vazyme). qRT-PCR was conducted using a Vazyme kit. Relative RNA expression levels of target genes were calculated using the 2^{-ΔΔCT} method. Primer sequences are listed in Supplementary Table S2.

Chromatin immunoprecipitation

Chromatin immunoprecipitation (ChIP) experiments were performed according to the ChIP-IT High Sensitivity Kit instructions (cat. #53040, Active Motif). Briefly, 100 million cells were cross-linked with 1% formaldehyde and sonicated on ice (10 minutes, 3 seconds on, 3 seconds off, 40% output). After centrifugation, the supernatant was collected, and DNA concentration was measured. The supernatant was incubated overnight at 4°C with anti-H3K181a (PTM-1406). The following day, the agarose beads were washed, and 30 µL of protein G agarose beads were added to each immunoprecipitation reaction, followed by incubation on a rotating shaker at 4°C for 3 hours. ChIP-DNA was eluted using filter columns and purified using purification columns. The purified DNA fragments were used to construct ChIP sequencing (ChIP-seq) libraries, which were amplified and sequenced on the HiSeq

2500 platform (Illumina). The primers used for qPCR analysis in this study are listed in Supplementary Table S2.

Conditioned medium preparation

Primary fibroblasts (2×10^6) were seeded in a 10 cm² culture dish and cultured in fibroblast medium. When the cells reached 70% confluence, they were washed twice with PBS and further cultured in fresh DMEM containing 10% FBS (SBI) for 48 hours. The medium (10^5 cells/mL) was then collected and centrifuged at $3,000 \times g$ for 10 minutes to remove cells and debris. The conditioned medium (CM) was either used immediately or stored at -80°C for subsequent stimulation of cancer cells (at a concentration of 5×10^5 cells/mL) or DRG cells.

Plasmid, siRNA, lentiviral transfection, and CRISPR-Cas9

All plasmids, siRNAs, lentivirus, and CRISPR-Cas9 used in this study were produced by GenCefe Biotech. The full-length human GAPDH, full-length human H3, GAPDH with lysine-to-arginine mutations (K66R, K139R, K186R, K263R), GAPDH with a lysine-to-glutamine mutation (K66Q), H3 with a lysine-to-arginine mutation (K18R), and H3 with a lysine-to-glutamic acid mutation (K18E) were cloned into the pcDNA3.1 expression vector. Additionally, the CRISPR cell line was constructed by GENEWIZ. To mediate GAPDH c.A196C c. A197G c.G198T (AAG>CGT, p.K66R) in the PANC1 cell line, the ribonucleoprotein complex was used. Briefly, Cas9 protein and single-guide RNA (sgRNA) were incubated at room temperature for 20 minutes, mixed with single-stranded oligonucleotides, followed by electrotransfection of a total of 3×10^5 TPC-1 cells, according to the manufacturer's instructions. After 48 hours of transfection, cells were diluted by a limited dilution method and seeded onto 96-well plates. Selection of individual clones was performed 2 to 4 weeks later, and the mutated clones were confirmed by PCR and Sanger sequencing. The sgRNA was designed using the online CRISPR design tool (Red Cotton, <https://en.rc-crispr.com/>), and the sequences of sgRNA and single-stranded oligonucleotides were listed in Supplementary Table S3. The short hairpin RNAs targeting monocarboxylate transporter 1 (MCT1) and P300 (sequences listed in Supplementary Table S4) were constructed using the pCDH-CMV-MCS-EF1-copGFP-T2A-Puro vector. Relevant plasmids were transfected using Lipofectamine 3000 and P3000 (Invitrogen), whereas Lipofectamine 3000 was used to transfect siRNAs to knock down the expression of MCT1 and MCT4 (sequences listed in Supplementary Table S4). Lentiviral transduction was performed according to the manufacturer's instructions, and cells were selected with puromycin (A3740, APEX-BIO) for 2 weeks.

Single-cell RNA-seq analysis

The raw count matrix of single-cell RNA sequencing (scRNA-seq) of PNI⁺ and PNI⁻ samples was obtained from previous studies (20, 21). Two PNI⁺ samples were downloaded from the Gene Expression Omnibus (GSE155698), whereas 6 PNI⁻ and 18 PNI⁺ samples were downloaded from Genome Sequence Archive (GSA: CRA001160). The raw count matrix and preliminary analyses of all samples were preprocessed using the R package Seurat (version 5.1.0). Briefly, the low-quality cells were filtered out using user-defined parameters (nFeature RNA >200, nFeature RNA <8,000, percent_mt < 10), which required at least 200 and no more than 8,000 RNAs, with less than 10% mitochondrial RNA. Then, the raw count matrix was normalized, and 2,000 high-variable genes were selected for sample integration using canonical correlation

analysis methods and principal component analysis. Subsequently, we obtained cell clustering using Uniform Manifold Approximation and Projection, and the cell clusters were identified using a marker gene list (Supplementary Tables S5 and S6). The differential expression genes among different cell clusters or different disease conditions were identified using the FindMarkers function in Seurat. The analysis of the subtype of fibroblast cells was carried out using the same method described above.

Spatial transcriptomics

Paraffin-embedded tissue was processed into an hematoxylin and eosin tissue microarray and placed on a Visium slide. After treatment with 0.1 N HCl and decross-linking buffer, the prehybridization and hybridization steps were performed following the Visium Spatial Gene Expression for formalin-fixed, paraffin-embedded (FFPE) reagent kit protocol (10x Genomics, User Guide CG000407 Rev C). Library preparation, including probe ligation, extension, and elution, was conducted per the manufacturer's instructions, and sequencing was performed on the NovaSeq 6000 (Illumina) with 28-bp read 1 and 91-bp read 2.

Sequenced libraries were processed using Space Ranger (version 2.0.0), aligning reads to the GRCh38 human reference genome. Tissue overlaying spots were identified and filtered, generating unique molecular identifier count matrices. Data analysis was performed in R using Seurat (version 4.1.0) with SCTransform normalization. Four sample matrices were merged, and 3,000 highly variable genes were selected for principal component analysis. The top 30 principal components were used for clustering and Uniform Manifold Approximation and Projection for Dimension Reduction visualization. The cell marker annotation tables used in spatial transcriptomics can be found in Supplementary Tables S5 and S6.

Mass spectrometry

Protein samples after coimmunoprecipitation (co-IP) were separated by SDS/PAGE and subjected to Coomassie blue staining. Differential bands were excised and sent to Wininnovate Bio for analysis. The lyophilized peptide fractions were reconstituted in ddH₂O containing 0.1% formic acid, and 2 μL aliquots were loaded onto a nanoViper C18 trap column (Acclaim PepMap 100, 75 $\mu\text{m} \times 2$ cm). Chromatographic separation was performed online using the EASY-nLC 1200 system (Thermo Fisher Scientific). The trapping and desalting steps were conducted with 20 μL of 100% solvent A (0.1% formic acid). The peptides were then eluted with a gradient of 5% to 38% solvent B (80% acetonitrile, 0.1% formic acid) over 60 minutes on an analytical column (Acclaim PepMap RSLC, 75 $\mu\text{m} \times 25$ cm, C18, 2 μm , 100 \AA). Tandem mass spectrometry data were acquired using data-dependent acquisition on a Thermo Fisher Q Exactive mass spectrometer equipped with a Nano Flex ion source. Data acquisition was performed with an ion spray voltage of 1.9 kV and an interface heater temperature of 275°C. The full mass spectrometry (MS) survey scan had a target value of 3×10^6 , with a scan range from 350 to 2,000 m/z, a resolution of 70,000, and a maximum injection time of 100 ms. For MS2 analysis, only ions with charge states of 2 to 5 were selected for fragmentation via higher-energy collision dissociation with a normalized collision energy of 28. The MS2 spectra were acquired in the ion trap in rapid mode, with an automatic gain control target of 8,000 and a maximum injection time of 50 ms. Dynamic exclusion was set to 25 seconds.

Isolation of Sprague-Dawley rat DRG and DRG cells

Neonatal Sprague-Dawley rats were euthanized, and the spine was isolated. DRGs were rapidly removed from the spine and transferred to F12 medium (Gibco) for further experiments. For DRG cell isolation, DRGs were digested with 2 mg/mL collagenase (Sigma Aldrich) and 2 mg/mL trypsin (Sigma Aldrich) at 37°C for 30 minutes, followed by filtration and centrifugation. The cell pellet was resuspended and cultured in a 37°C, 5% CO₂ incubator for further analysis.

Neural invasion model *in vitro*

For CM treatment, PANC1 cells (with or without MCT1 knockdown) were cultured for 2 weeks in conditioned media derived from CAFs [non-PNI-associated CAFs (npCAF), PNI-associated cancer-associated fibroblasts (pCAF), or MCT4-knockdown CAFs], with the medium being refreshed every other day. The cells were then collected for further analysis. To assess neurite outgrowth of DRG cells, pretreated PANC1 cells (2×10^5) were seeded into the upper chamber of a six-well transwell insert with a pore size of 0.4 μm . The medium was supplemented with or without L-lactate (20 mmol/L, cat. #L6402, Sigma-Aldrich) and 2DG (4 mmol/L, D6134, Sigma-Aldrich). Primary DRG cells (2×10^5) were seeded into the lower chamber, and neurite outgrowth was monitored using a phase-contrast microscope.

For migration and invasion assays, pretreated PANC1 cells were seeded into the upper chamber (coated with or without Matrigel, BD Biosciences) in 200 μL of serum-free DMEM (with or without L-lactate, 20 mmol/L, cat. #L6402, Sigma-Aldrich, and 2DG, 4 mmol/L, D6134, Sigma-Aldrich). Primary DRG cells were seeded into the lower chamber with 600 μL of DMEM containing 10% FBS. After 12 hours of incubation, noninvasive cells on the upper surface of the insert were removed, and invasive cells on the lower surface were fixed and stained with crystal violet. The number of stained cells was counted under a light microscope to determine neural invasion capability.

For 3D coculture and DRG analysis, tumor cells were resuspended in Matrigel at a concentration of 10^4 cells/ μL , and 20 μL of this cell mixture was seeded into each well of a six-well plate. DRGs isolated from neonatal mice were seeded in 20 μL of Matrigel (Invitrogen) at a distance of 2 mm from the tumor cells. After solidification, the specified CM was added, and the medium was refreshed every 2 days. Images were captured on days 1 and 7 using a light microscope (Invitrogen). The neural invasion index was calculated as follows: $1 - (\text{the distance from tumor cells to DRG on day 7}) / (\text{the distance from tumor cells to DRG on day 1})$.

Animal experiments

PANC1 cells were cultured for 14 days in CM derived from wild-type (WT) pCAF or GAPDH K66R-mutant CAFs or were subjected to MCT1 knockdown using short hairpin RNA or left untreated. Four-week-old BALB/c nude mice ($n = 10$) were anesthetized, and the sciatic nerve was surgically exposed. Tumor cells (1×10^4 cells/ μL , 2 μL per injection) were injected into the right sciatic nerve of BALB/c-nu/nu mice using a Hamilton syringe, whereas 2 μL of PBS was injected into the left sciatic nerve as a control. Mice injected with wild-type PANC1 cells were injected intraperitoneally with 2DG (500 mg/kg; Sigma-Aldrich, D6134) or administered sodium lactate (1 g/kg) daily via i.p. injection. Sciatic nerve function was monitored weekly, with a scoring range from 4 (normal) to 1 (completely paralyzed paw). The sciatic nerve index was measured biweekly by assessing the distance between the first and fifth toes of the hind limb. After 6 weeks, all mice were sacrificed, and the sciatic

nerves and tumor specimens were harvested and fixed for histologic analysis. This study was approved by the Ethical Committee of Guangdong Provincial People's Hospital. All animal experiments (Approval no. KY2024-999-01) conducted were compliant with the Ethical Committee of Guangdong Provincial People's Hospital.

Genetically engineered mouse model

KPC (LSL-KRAS^{G12D/+}, LSL-TRP53^{R172H/+}, PDX-1-CRE^{+/+}) mice were purchased from Shanghai Model Organisms. Mice were administered sodium lactate (1 g/kg, $n = 10$) daily via i.p. injection, AZD3965 (100 mg/kg, S7339, Selleckchem, $n = 10$) orally daily, and 1 mg/kg heptelidic acid (cat. #C4003, APExBIO, $n = 10$) intraperitoneally three times a week. After 4 weeks, all mice were sacrificed, and the pancreas was harvested and fixed for histologic analysis. This study was approved by the Ethical Committee of Guangdong Provincial People's Hospital. All animal experiments (Approval no. KY2024-999-01) conducted were compliant with the Ethical Committee of Guangdong Provincial People's Hospital.

RNA extraction, library construction, and Illumina sequencing

Total RNA was extracted from cells using TRIzol reagent (Invitrogen). RNA library construction and sequencing were performed by Guangzhou IGE Biotechnology Ltd. The experimental process is briefly described as follows: Total RNA was extracted and quality-checked, and then eukaryotic mRNA was enriched using magnetic beads with oligo (dT). Fragmentation reagent was added to break the mRNA into short fragments, followed by first-strand cDNA synthesis using the fragmented mRNA as a template. Second-strand cDNA synthesis was then performed, and the resulting cDNA was purified, end-repaired, A-tailed, and ligated to sequencing adapters. The fragments were size-selected and PCR-amplified to construct the library. The constructed library was quality-checked using an Agilent 2100 Bioanalyzer and Qubit, and sequencing was performed using an Illumina sequencer.

Statistical analysis

Statistical analyses were conducted using SPSS version 13.0 and GraphPad Prism version 9.0. Quantitative data are generally expressed as mean \pm SD from three independent experiments, unless otherwise specified. For comparisons between two groups, the Student *t* test or the nonparametric Mann–Whitney *U* test was employed, depending on data distribution. For multiple group comparisons, one- or two-way ANOVA was used, followed by Tukey multiple comparison test to evaluate differences between all group pairs. Nonparametric variables were analyzed using the χ^2 test or Fisher exact test. Spearman correlation was applied to assess the relationship between two continuous variables. The Cox proportional hazards model was utilized to obtain the likelihood ratio *P* value, and Kaplan–Meier survival curves were generated using the survival package. The relationship between tissue lactate levels, αSMA , pan-lactylation expression, H3K18la, LICAM, SLIT1 expression, and overall survival as well as DFS was examined using a multivariate Cox regression model. A *P* value < 0.05 was considered statistically significant.

Data availability

The transcriptomic data and ChIP-seq data generated in this study are publicly available in the Gene Expression Omnibus at accession numbers GSE290845 and GSE290654, respectively. All other raw data are available from the corresponding author upon request.

Results

The role of pCAFs in promoting neural invasion in pancreatic cancer

To explore the diverse roles of CAFs in the neural invasion of pancreatic cancer, we isolated CAFs from patients exhibiting severe neural invasion, termed pCAFs, and from those without neural invasion, referred to as npCAFs. We confirmed the characteristics of CAFs using morphologic analysis, Western blotting, immunofluorescence, and flow cytometry. The results demonstrated that primary CAFs exhibited a spindle-shaped or triangular morphology and highly expressed PDPN and fibroblast activation protein (FAP) markers (Supplementary Fig. S1A–S1C). Flow cytometry results demonstrated that the CAFs were negative for EpCAM (epithelial cell marker), CD31 (endothelial cell marker), and CD45 (lymphocyte marker; Supplementary Fig. S1D). These cells were then cocultured with pancreatic cancer cell lines for 2 weeks. Tumor cells cocultured with pCAFs demonstrated enhanced neurite outgrowth and invasive capabilities compared with those cocultured with npCAFs or maintained in monoculture (Fig. 1A–C). Additionally, DRG coculture assays highlighted that pCAF supernatants notably enhanced the neural invasion properties of pancreatic cancer cells, unlike npCAF supernatants (Fig. 1D and E). This phenomenon was corroborated *in vivo* using a mouse sciatic nerve invasion model. PANC1 cells were precultured with pCAFs or npCAFs for 2 weeks and then injected into the sciatic nerves of nude mice. Tumor cells associated with pCAFs induced severe hind limb paralysis, evidenced by a marked reduction in hind paw width (Fig. 1F–I).

Metabolic reprogramming in pCAFs

To provide a detailed insight into the roles of pCAFs and npCAFs in PNI, we analyzed single-cell sequencing data from 27 PDAC tumor samples categorized based on the presence or absence of PNI (20, 21). Following initial quality control, we acquired single-cell transcriptomes encompassing 37,063 cells from PDAC samples with PNI and 6,774 cells from PDAC samples without PNI and identified 16 main clusters (Fig. 2A). We identified cluster-specific marker genes through differential gene expression analysis to characterize each cell cluster (Fig. 2B). Notably, the enrichment of fibroblasts was significantly increased in PDAC samples with PNI compared with those without PNI, consistent with our previous reports (Fig. 2C and D). KEGG analyses revealed a significant enrichment of the glycolytic pathway in fibroblasts in PNI (Fig. 2E). CAFs exhibit substantial heterogeneity and plasticity, affecting tumor progression in divergent ways. To identify classical CAF subtypes contributing to PNI in PDAC, we reclustered fibroblasts in PDAC. This analysis revealed an increased prevalence of the myofibroblastic cancer-associated fibroblast (myCAF) cluster and a reduction in inflammatory CAF (iCAF) clusters in PNI-positive PDAC compared with those without PNI (Fig. 2F and G). KEGG analysis demonstrated a significant enrichment of the glycolytic pathway in myCAF compared with iCAF (Fig. 2H). Then we conducted IF analyses on iCAF and myCAF subpopulations in patients with and without severe PNI (iCAF: PDPN⁺IL6⁺; myCAF: PDPN⁺αSMA⁺). The results revealed that myCAF predominated in tissues from patients with severe neural invasion, whereas iCAF were more common in patients without significant PNI (Fig. 2I). To further characterize CAF heterogeneity, we reanalyzed scRNA-seq data using unsupervised dimensionality reduction. The results revealed that clusters 0, 1, 3, and 4 exhibited myCAF characteristics, with clusters 0 and 4 significantly enriched for glycolysis-related genes

(Supplementary Fig. S2A and S2B). Additionally, we observed that clusters 0 and 4 were more prevalent in PNI-positive patients compared with those without PNI (Supplementary Fig. S2C). Using a pseudotime analysis with selected glycolysis-related genes, we observed a gradual decline in glycolytic activity from states 1 to 4. Importantly, clusters 0 and 4 were predominantly present in state 1 (Supplementary Fig. S2D and S2E). Then, we used FAP as a marker to magnetically enrich pan-CAFs from both PNI-positive and PNI-negative patients and performed scRNA-seq. The results were consistent with our original tissue-derived single-cell sequencing findings. Single-cell analysis revealed that the purity of CAFs exceeded 95% (Supplementary Fig. S3A). The proportion of myCAFs was significantly higher in PNI-positive patients compared with PNI-negative ones (Supplementary Fig. S3B–S3D). The glycolytic pathway was markedly activated in myCAFs compared with iCAFs (Supplementary Fig. S3E). Unsupervised dimensionality reduction analysis revealed that clusters 2, 3, 4, 5, 6, 7, and 9 exhibited myCAF characteristics (Supplementary Fig. S3F and S3G). Among these, clusters 3, 4, and 6 were significantly enriched for glycolysis-related genes and were more prevalent in PNI-positive patients (Supplementary Fig. S3H and S3I). To evaluate the spatial localization of iCAF and myCAF in the PNI region, spatial transcriptomics were conducted in pancreatic cancer tissue sections. The spots were classified into 13 clusters (Supplementary Fig. S4A). Notably, myCAF clusters were predominantly situated in the PNI region (Supplementary Fig. S4B–S4D). GESA revealed that the glycolysis pathway was enriched in myCAF relative to iCAF (Supplementary Fig. S4E).

We noted a color shift from pink to orange in the culture medium of pCAFs, alongside a significant pH reduction compared with npCAFs. These findings imply that pCAFs secrete higher levels of acidic catabolites than npCAFs. Subsequently, mRNA sequencing was performed on pCAFs and npCAFs. Gene set enrichment analysis highlighted a substantial activation of glycolysis in pCAFs relative to npCAFs (Supplementary Fig. S5A and S5B). Measurements of glucose uptake, lactate production, and oxygen consumption revealed that pCAFs exhibited significantly higher lactate production and increased glucose uptake compared with npCAFs (Supplementary Fig. S5C–S5F). Moreover, mitochondrial function related to oxidative phosphorylation was impaired in pCAFs. Pretreatment with the glycolysis inhibitor 2DG markedly impaired the ability of pCAFs to enhance neurite outgrowth and invasion in pancreatic cancer cells (Supplementary Fig. S5G–S5I). This phenomenon was similarly validated in animal experiments. We treated pCAFs with 2DG *in vitro* and then collected these 2DG-treated pCAFs for coculture with PANC1 cells for 2 weeks. Then, PANC1 cells were collected to establish a sciatic nerve model. 2DG treatment of pCAFs weakened the ability of pCAFs to promote PANC1 cell neural invasion, characterized by a reduction in hind limb paralysis (Supplementary Fig. S5J–S5L). To investigate whether LIF can be produced by pCAFs, we compared the expression and secretion of LIF among pCAFs, iCAFs, and myCAFs using Western blot and ELISA assays. The results showed that LIF expression and secretion were significantly higher in iCAFs compared with pCAFs and myCAFs (Supplementary Fig. S5M–S5O).

GAPDH acetylation regulates metabolic reprogramming in pCAFs

To investigate the mechanism behind this metabolic reprogramming, we evaluated the expression levels of key glycolytic enzymes in pCAFs and npCAFs. Western blot and PCR analyses revealed no alterations in the expression levels of these enzymes

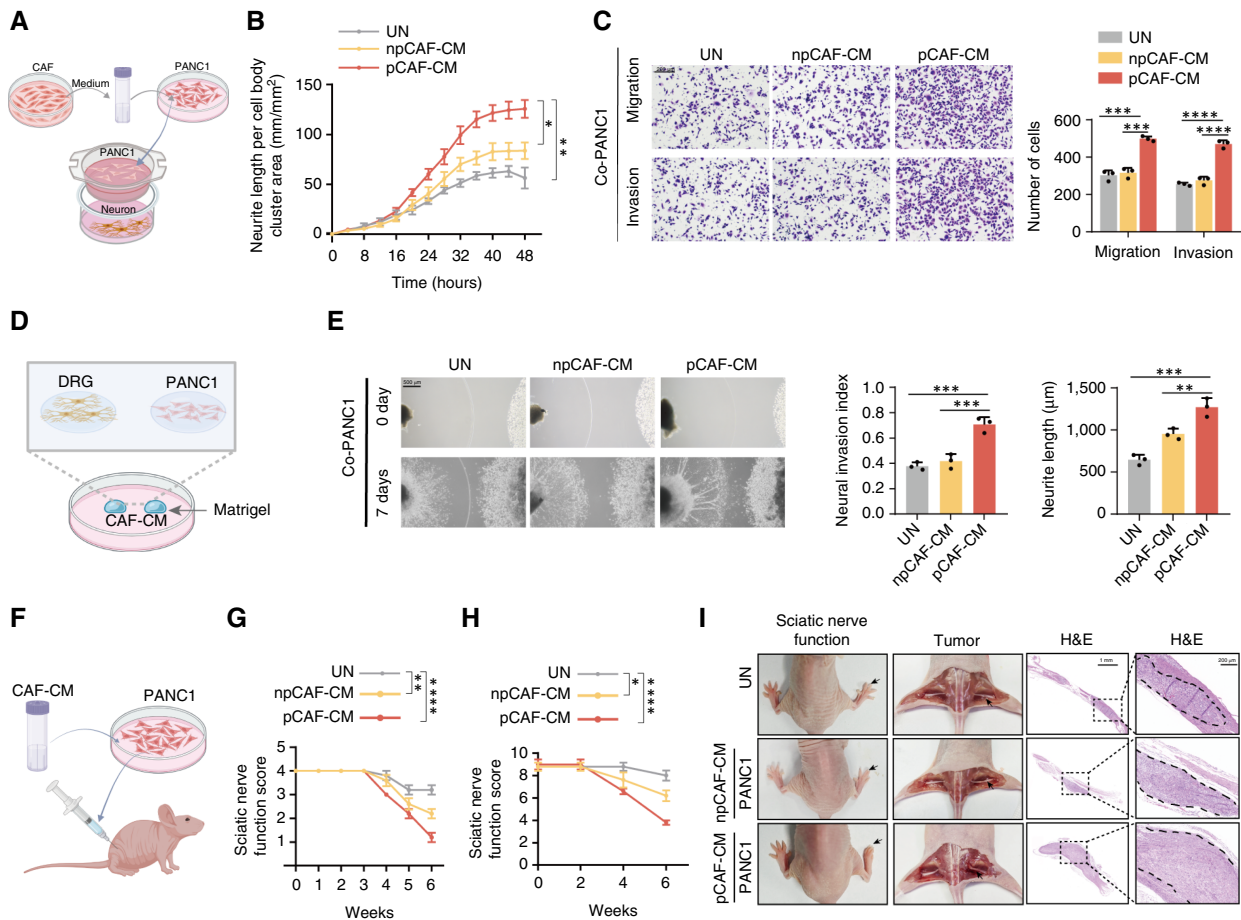


Figure 1.

The role of pCAFs in promoting neural invasion in pancreatic cancer. **A**, Schematic illustration of the Transwell coculture system for neuronal and tumor cells. Tumor cells were pretreated with fibroblast-derived CM. **B**, Quantitative analysis of neurite length in neuronal cells cultured in the Transwell system with npCAF or pCAF-CM. Phase contrast images were captured every 4 hours. UN, untreated cancer cells. $n = 3$ independent experiments; one-way ANOVA test; data are shown as the means \pm SD. **C**, Representative image (left) and quantitative analysis (right) of PANC1 cell migration and invasion in the Transwell system following treatment with npCAF or pCAF-CM. Scale bars, 200 μ m ($n = 3$ independent experiments; one-way ANOVA test; data are shown as the means \pm SD). **D**, Schematic illustration of the 3D coculture system of tumor cells and DRG. Tumor cells were pretreated with fibroblast-derived culture medium. **E**, Left, representative image of a coculture of murine DRG with PANC1 cells treated with npCAF or pCAF culture medium. Right, quantitative analysis of the neuroinvasive ability of PANC1 cells. Scale bar, 500 μ m. $n = 3$ independent experiments; one-way ANOVA test; data are shown as the means \pm SD. **F**, Diagram showing the setup of sciatic nerve invasion models. PANC1 cells were pretreated with culture medium derived from npCAF or pCAF and then injected into the sciatic nerves of nude mice ($n = 5$ mice per group). **G**, Hind limb function was assessed weekly by scoring sciatic nerve function ($n = 10$ mice per group; Kruskal-Wallis test with Dunn multiple comparisons test; data are shown as the means \pm SD). **H**, Sciatic nerve function was assessed every 2 weeks by determining the sciatic nerve index ($n = 10$ mice per group; Kruskal-Wallis test with Dunn multiple comparisons test; data are shown as the means \pm SD). **I**, Gross and surgical images, hematoxylin and eosin (H&E) staining images of sciatic nerve invasion. The dotted line represents the boundary of the tumor. Scale bar, 1,000 μ m. *, $P < 0.05$; **, $P < 0.01$; ***, $P < 0.001$; ****, $P < 0.0001$.

(Fig. 3A and B). We then assessed their functional activity, finding that GAPDH functional activity was significantly elevated in pCAFs compared with npCAFs (Fig. 3C). Previous studies have demonstrated that acetylation modifications significantly influence the enzymatic activity of GAPDH (22, 23). To explore the role of acetylation modifications, lysates from pCAFs and npCAFs were analyzed by Western blot using an acetylated-lysine-specific antibody (Fig. 3D). The most prominent band at approximately 35 to 40 kDa was validated as GAPDH via mass spectrometry (Supplementary Fig. S6A and S6B). Co-IP assays confirmed that the acetylation level of GAPDH was higher in pCAFs than in npCAFs (Fig. 3E).

Next, we employed an acetyl proteomic approach to identify acetylation sites within GAPDH. Following immunoprecipitation, GAPDH was analyzed using LC/MS. Four acetylation sites were identified as Lys66, Lys139, Lys186, and Lys263 (Fig. 3F; Supplementary Fig. S6C–S6F). To assess the impact of these acetylation sites on GAPDH activity, we substituted lysine at positions 66, 139, 186, or 263 with arginine to simulate a nonacetylated state (K66R, K139R, K186R, K263R) and then assayed the enzymatic activities of these GAPDH variants *in vitro*. Notably, the K66R mutation, unlike the other mutations, significantly reduced GAPDH activity compared with the wild type (Fig. 3G). The Lys66 residue, exclusively acetylated in pCAFs, is conserved across

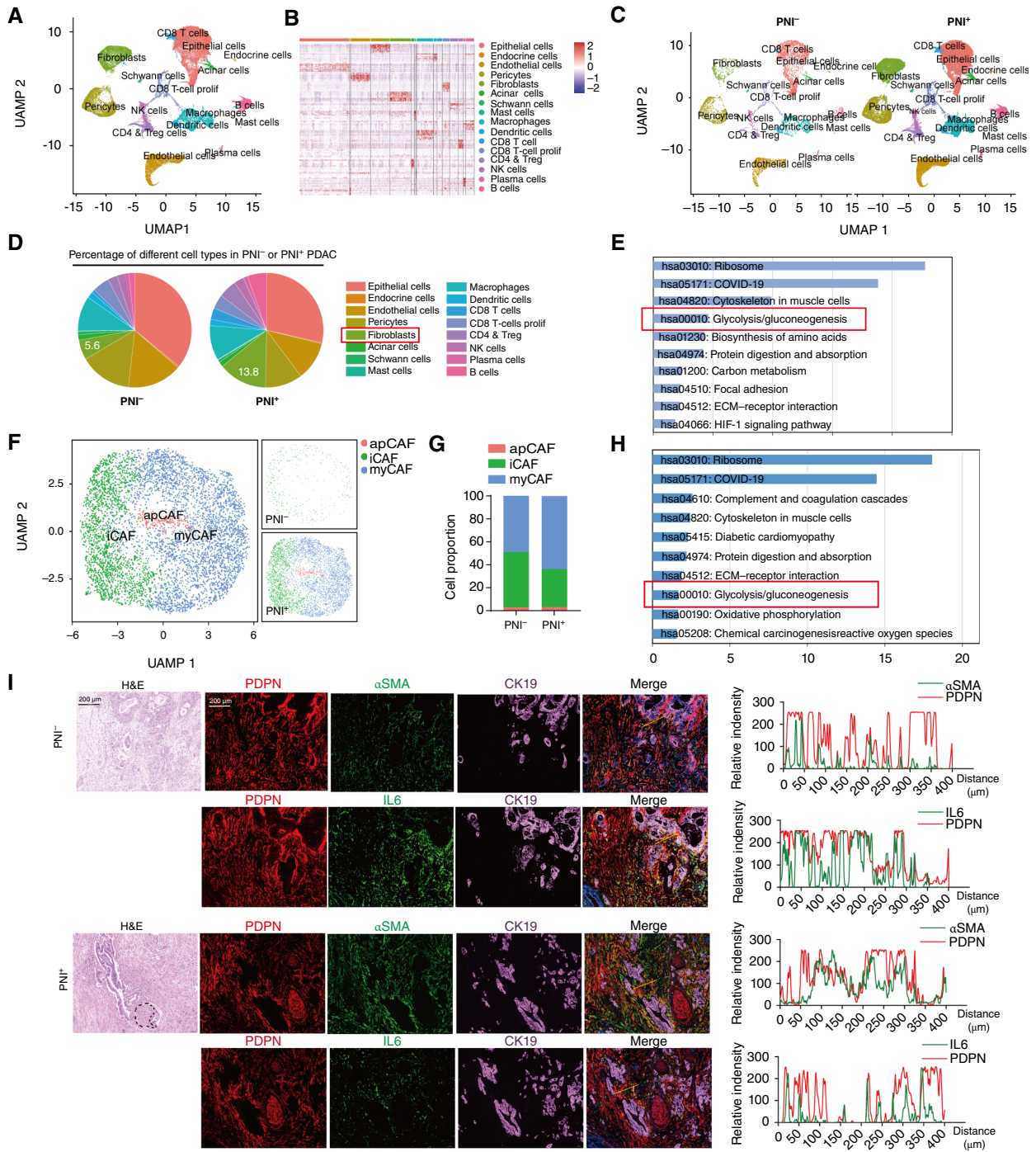


Figure 2.

Metabolic reprogramming in pCAFs. **A**, Uniform Manifold Approximation and Projection (UMAP) plots of single cells identified by scRNA-seq, colored by major cell types. **B**, Heatmap displaying the most differentially expressed genes across each major cell type. **C** and **D**, UMAP plots and pie charts showing the distribution of different cell types in PDAC tissues with or without PNI. **E**, KEGG functional enrichment analysis of signaling pathway in CAFs from PDAC tissues with or without PNI. **F** and **G**, UMAP plots and bar plots displaying the reclustering of fibroblasts in scRNA-seq data from PDAC tissues with and without PNI. **H**, Gene set enrichment analysis of the glycolysis pathway comparing myCAFs with other CAF subtypes. **I**, Left, representative images of mIF staining for PDPN, αSMA, and CK19 in PDAC tissues with (PNI+) and without neural invasion (PNI-). PDPN was used as a pan-CAF marker, αSMA was used as a myCAF marker, IL6 was used as an iCAF marker, and CK19 was used as a tumor marker. The corresponding intensity plots of regions of interest (straight yellow lines) in the mIF image are displayed on the right, respectively. Red curves, PDPN relative fluorescence intensity; green curves, αSMA or IL6 relative fluorescence intensity. The red-green overlap represents the colocalization of PDPN with αSMA or IL6. Higher peak intensity indicates stronger fluorescence expression. The dotted line represents the boundary of the tumor. ImageJ was used to quantify fluorescence intensity in these areas. Scale bars, 200 μm.

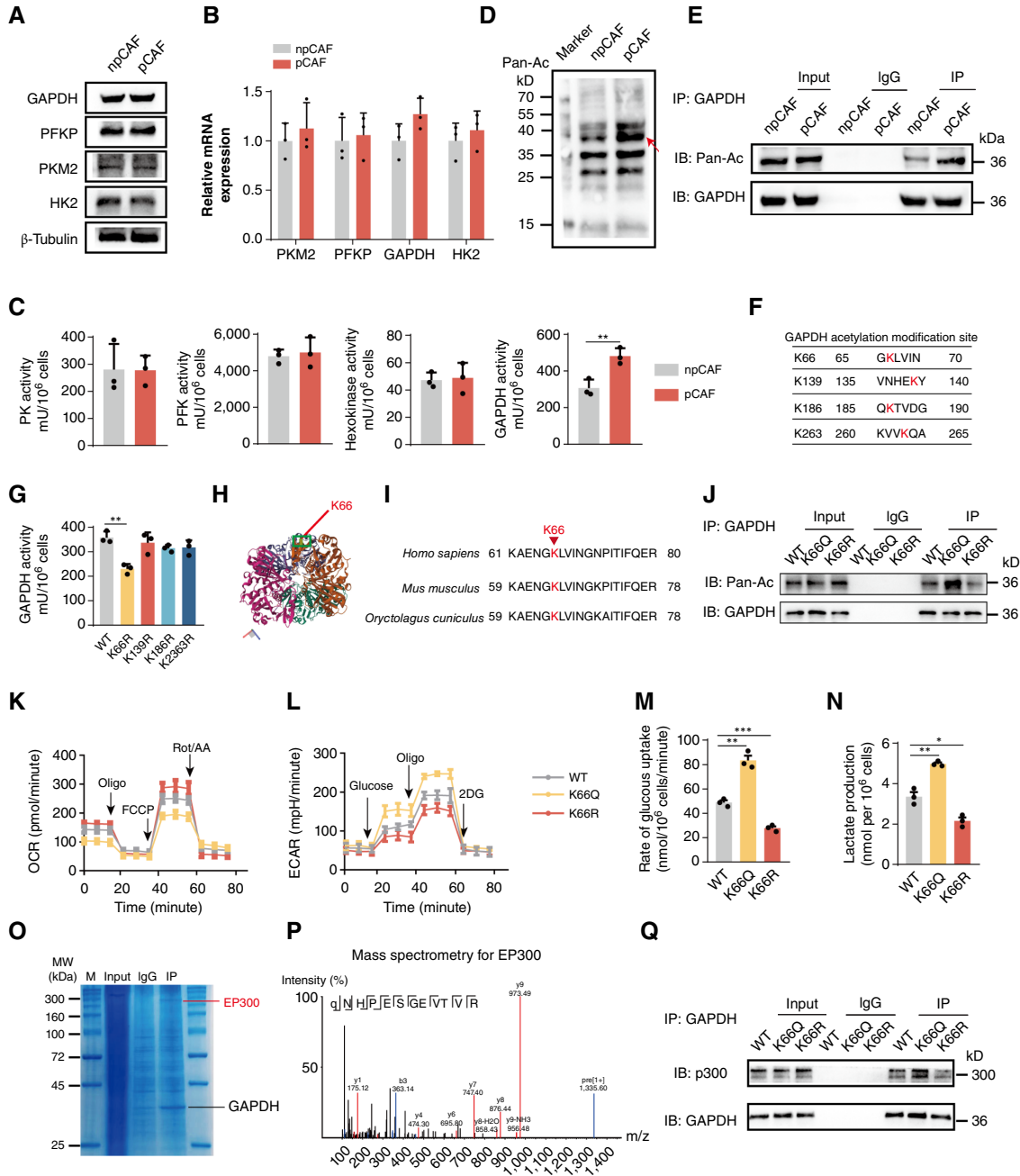


Figure 3.

GAPDH acetylation regulates metabolic reprogramming in pCAFs. **A**, Western blot of the expression of GAPDH, PFKP, PKM2, and HK2 in npCAF or pCAF. **B**, qRT-PCR analysis of *GAPDH*, *PFKP*, *PKM2*, and *HK2* in npCAF or pCAF. **C**, The enzyme activity of pyruvate kinase (PK), phosphofruktokinase (PFK), hexokinase, and GAPDH in npCAF or pCAF. **D**, Pan-acetylation level was analyzed by immunoblotting with an anti-acetyl lysine antibody. **E**, An immunoprecipitation blot showing the GAPDH acetylation level, using a GAPDH antibody *in vitro*. **F**, The GAPDH acetylation modification site (red). **G**, The enzymatic activities of GAPDH variants (K66R, K139R, K186R, K263R) *in vitro*, with lysine (K) at positions 66, 139, 186, or 263 with arginine (R) to simulate a nonacetylated state. **H**, Three-dimensional stereostructure of GAPDH, with the green box representing K66. **I**, The K66 site in GAPDH is conserved across species. Alignment shows lysine residues corresponding to human GAPDH K66, highlighted in red. **J**, Effect of different GAPDH K66 mutations on acetylation levels. K66Q indicates that the lysine at position 66 is substituted by glutamine. K66R indicates that the lysine at position 66 is substituted by arginine. **K–N**, Effects of GAPDH K66 on aerobic glycolysis. The GAPDH K66 wild-type or K66-mutant pCAFs were assessed for oxygen consumption rate (OCR) as an indicator of oxidative phosphorylation and deduced levels of basal respiration and ATP production (**K**). Rot/AA, combination of rotenone and antimycin A. The ECAR was used to assess glycolytic flux and glycolytic capacity (**L**). The rate of glucose uptake (**M**) and lactate production (**N**) were analyzed in GAPDH K66 WT or K66-mutant pCAF. **O**, Representative Coomassie Aram staining image of GAPDH-associated proteins in pCAFs. The red line indicates the bands corresponding to distinct proteins enriched by GAPDH that were analyzed by LC-MS. **P**, MS identification of GAPDH-binding proteins. The red line indicates the bands corresponding to distinct proteins enriched by GAPDH that were analyzed by LC-MS. **Q**, The *in vitro* interactions of P300 and GAPDH were detected by immunoprecipitation. *, $P < 0.05$; **, $P < 0.01$; ***, $P < 0.001$.

many species (Fig. 3H and I). To further elucidate the functional significance of Lys66 in glycolytic enzyme activity, we substituted lysine at position 66 with glutamine (K66Q) to simulate an acetylated state. We used CRISPR-Cas9 to mutate GAPDH K66 to K66R and K66Q in pCAFs. This led to elevated acetylation levels in the K66Q variant, whereas acetylation levels were reduced in the K66R variant (Fig. 3J). In the GAPDH K66R-expressing cells, glucose uptake, lactate production, and oxygen consumption were significantly reduced compared with cells expressing wild-type GAPDH. Conversely, the GAPDH K66Q-mutant cells exhibited the opposite effect (Fig. 3K–N). These findings collectively indicate that Lys66 acetylation plays a crucial role in the enzymatic activity of GAPDH.

Subsequently, we explored which acetyltransferase is responsible for the acetylation of GAPDH by applying co-IP combined with mass spectrometry. Among the 20 potential binding proteins of GAPDH, P300, a key acetyltransferase, was identified with high confidence as a potential protein responsible for the acetylation of GAPDH. Western blot and qRT-PCR assays showed that P300 expression levels were not significantly different between pCAFs and npCAFs (Supplementary Fig. S6G and S6H). However, enzymatic activity assays revealed that P300 enzymatic activity was higher in pCAFs than in npCAFs (Supplementary Fig. S6I). Previous studies have reported that AKT-mediated phosphorylation of P300 can affect its enzymatic activity (24). Western blot revealed that expression levels of p-mTOR, pAKT, and p-P300 were elevated in pCAFs compared with npCAFs (Supplementary Fig. S6J and S6K). Inhibition of AKT reduced P300 phosphorylation and enzymatic activity (Supplementary Fig. S6L and S6M). We confirmed the interaction between P300 and GAPDH in pCAFs by immunoprecipitation (Fig. 3O–Q). Furthermore, the *in vitro* binding assay demonstrated a direct interaction between P300 and GAPDH (Supplementary Fig. S6N). To confirm the P300 is responsible for the increased acetylation of GAPDH, we knocked down *EP300* expression in pCAFs via shP300. Co-IP assays revealed that silencing P300 reduced the acetylation level of GAPDH in pCAFs (Supplementary Fig. S6O). Additionally, we treated cells with the bromodomain-specific inhibitor (CBP112), which selectively inhibited P300 acetylation activity. Co-IP assays further showed that the inhibition of EP300 bromodomain also suppressed GAPDH acetylation levels (Supplementary Fig. S6P). The co-IP assay demonstrated that AKT inhibition decreased the acetylation level of GAPDH (Supplementary Fig. S6Q). Previous studies have reported that TGF β can activate the mTOR/Akt signaling pathway (25). Consistently, our Western blot results showed that exogenous TGF β treatment of npCAFs upregulated the mTOR/AKT/P300 signaling pathway, leading to increased GAPDH acetylation (Supplementary Fig. S6R–S6T). The expression level of TGF β 1 in PNI⁺ patient tissues was also higher (Supplementary Fig. S6U). Collectively, these data indicate that activation of the TGF β /mTOR/AKT signaling pathway in pCAFs mediates P300 phosphorylation, enhances P300 enzymatic activity, and subsequently alters GAPDH acetylation levels.

pCAF-derived lactate influences PNI in pancreatic cancer

Given the elevated acidification indicated by ECAR and pH measurements of the CM, we speculated that pCAFs create an acidic microenvironment through a reprogrammed metabolism characterized by increased secretion of acidic metabolites. To identify the specific acidic metabolites responsible for enhanced PNI in pCAF-derived CM, we analyzed the metabolite profiles of pCAFs and npCAFs using nontargeted metabolic profiling. We selected the top four metabolites with the most significant expression differences in pCAFs as candidates and treated pancreatic cancer cells with these metabolites. Among these candidates, only lactate significantly

promoted pancreatic cancer PNI, whereas the other metabolites had no such effect (Supplementary Fig. S7A–S7C). Notably, lactate levels were significantly higher in the pCAF and predominantly concentrated within the glycolytic metabolic pathway (Fig. 4A–C). Correlation analysis revealed that there is a strong positive correlation between cell number and lactate production, as well as between tissue lactate levels and α SMA fluorescence intensity (Fig. 4D and E). Neurite outgrowth assays revealed that neurites in cultures treated with lactate were significantly longer than those in control cultures (Fig. 4F). Lactate substantially increased tumor invasion and migration capabilities compared with control groups (Fig. 4G). Additionally, DRG coculture experiments showed that lactate markedly enhanced the neural invasion capabilities of pancreatic cancer cells (Fig. 4H). Interestingly, when the lactate secretion transporter MCT4 in CAFs or the lactate uptake transporter MCT1 in tumor cells was knocked down, lactate did not enhance their neurotrophic capabilities (Fig. 4H). These findings suggest that lactate plays a central role in pCAF-regulated neural invasion.

pCAF-derived lactate regulates PNI through H3K18la

Lactate serves as a critical substrate for histone lactylation. We assessed protein lactylation levels in pancreatic cancer cells either cocultured with pCAFs or npCAFs. We observed that not all tumor cell lines have the same response to lactate treatment. Western blot assays indicated that global lactylation levels were elevated in cells cocultured with pCAFs compared with those cocultured with npCAFs (Fig. 5A). We observed that after treatment with the same concentration of lactate, intracellular lactate levels were higher in PANC1 cells and MiaPaCa-2 cells than in BxPC-3 cells (Supplementary Fig. S8A). Previous studies have reported that MCT1 is responsible for lactate uptake (26, 27). Western blot analysis indicated that the expression levels of MCT1 were higher in PANC1 cells and MiaPaCa-2 cells than in BxPC-3 cells, which may lead to the distinct responses observed in different tumor cell lines (Supplementary Fig. S8B). Intriguingly, IF staining revealed that lactylated proteins predominantly localized in the nucleus, with the most significant band appearing near 15 kDa on Western blots (Fig. 5A and B). Subsequent silver staining and mass spectrometry analysis after immunoprecipitation of lactylated proteins identified this band as histone H3 (Fig. 5C). We investigated various lactylation sites on histone H3 and observed that H3K18la levels gradually increased in tumor cells cocultured with pCAFs (Fig. 5D). IF confirmed that H3K18la levels were higher in cells cocultured with pCAFs compared with those cultured with npCAFs (Fig. 5E). Additionally, to further elucidate the functional significance of H3 Lys18 in pancreatic cancer neural invasion, we replaced lysine at position 18 with arginine (K18R) to mimic a delactylated state and with glutamic acid (K18E) to mimic a lactylated state (Fig. 5F). We discovered that inhibiting H3K18la levels curtailed both PNI and neurite outgrowth capabilities of tumor cells. Conversely, the H3K18E mutation showed the opposite effect (Fig. 5G–I). Moreover, we assessed global lactylation and H3K18la levels in patients with varying degrees of PNI. IF staining indicated significantly higher levels of global lactylation and H3K18la in patients with severe PNI, and merged confocal images confirmed that lactylation was localized to the nuclei of tumor cells in the PNI region (Fig. 5J and K). Collectively, these findings underscore that histone lactylation and H3K18la contribute to PNI in pancreatic cancer.

H3K18la activates L1CAM and SLIT1 transcription in pancreatic cancer

Histone lactylation plays a critical role in the transcriptional regulation of target genes. We conducted ChIP-seq using anti-

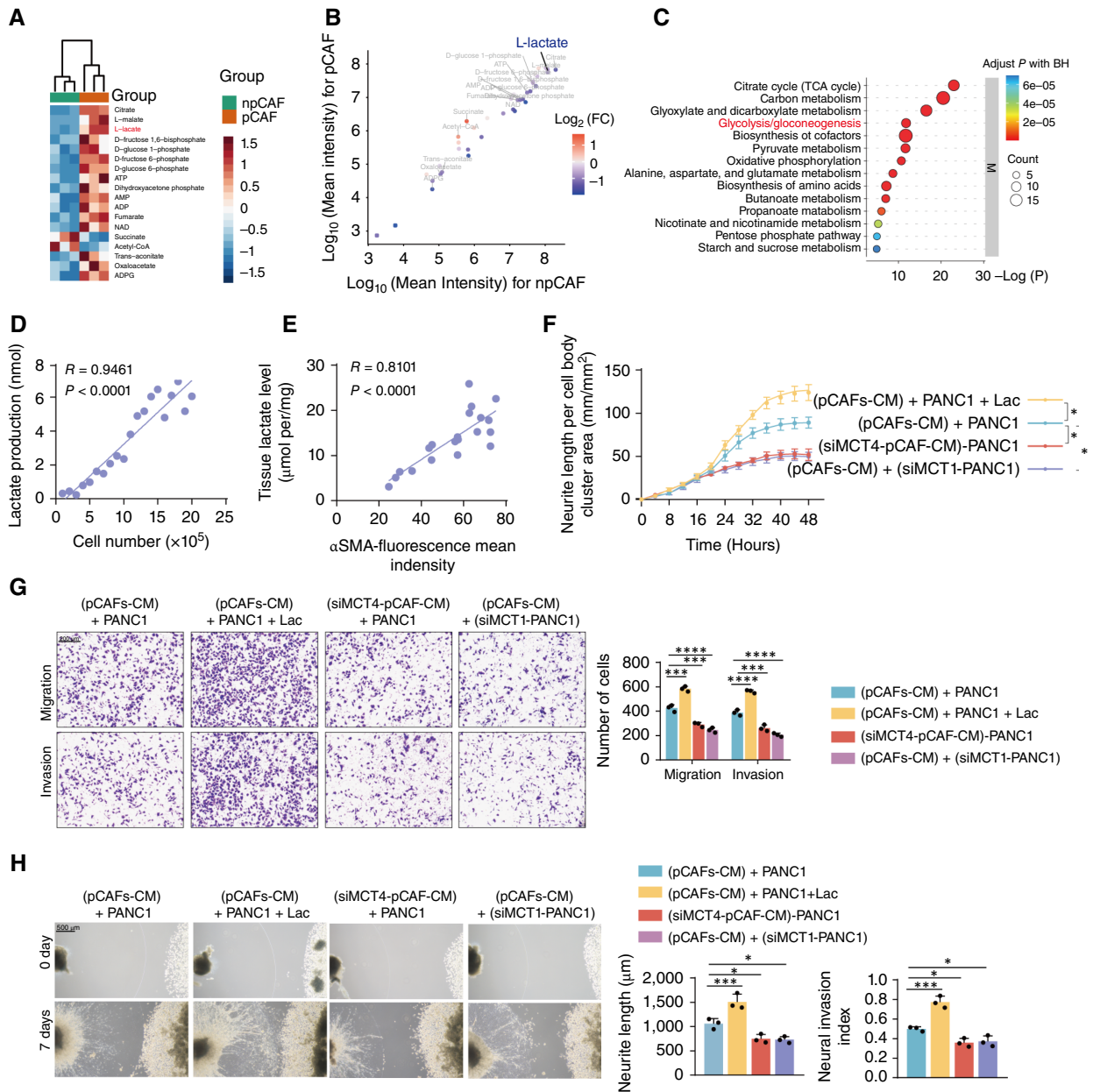


Figure 4.

pCAF-derived lactate influences perineural invasion in pancreatic cancer. **A** and **B**, Heatmap scatter plot showing the relative abundance of metabolites between npCAFs and pCAFs groups. BH, Benjamini-Hochberg; FC, fold change. **C**, Pathway enrichment analysis indicating upregulated metabolic pathways in pCAFs. The size of the dots represents the number of metabolites involved, and the color indicates the adjusted *P* values. **D**, Correlation between cell number and lactate production in pCAFs. The *R* values and *P* values were determined by Pearson correlation analysis. **E**, Correlation between αSMA fluorescence intensity and lactate production in PDAC tissues, $n = 20$. The *R* values and *P* values were determined by Pearson correlation analysis. **F**, Neurite length within the Transwell system was quantitatively analyzed under the indicated treatment. PANC1 cells under CM from pCAFs (pCAF_s-CM) alone, or pCAFs with siMCT1 treatment (siMCT4-pCAF_s-CM) or tumor cell culture medium with lactate supplementation or PANC1 with MCT1 depletion. Phase contrast images of neuronal cells were captured at 4-hour intervals ($n = 5$ independent experiments; one-way ANOVA test; data are shown as the means \pm SD). **G**, Representative image (left) and quantitative analysis (right) of PANC1 cell migration and invasion in the Transwell system with the indicated treatment. Scale bar, 200 μm . $n = 3$ independent experiments; one-way ANOVA test; data are shown as the means \pm SD. **H**, Neuroinvasive capacity of PANC1 cells following the specified treatment. Scale bar, 500 μm . $n = 3$ independent experiments; one-way ANOVA test; data are shown as the means \pm SD. *, $P < 0.05$; ***, $P < 0.001$; ****, $P < 0.0001$.

H3K18la antibodies to delineate the regulatory role of H3K18la in gene expression in PANC1 cells treated with lactic acid. This analysis revealed a pronounced enrichment of H3K18la in cells

exposed to lactate as opposed to untreated cells, with a significant proportion of H3K18la-binding peaks localized within promoter sequences (≤ 3 Kb), suggesting a potential regulatory role in gene

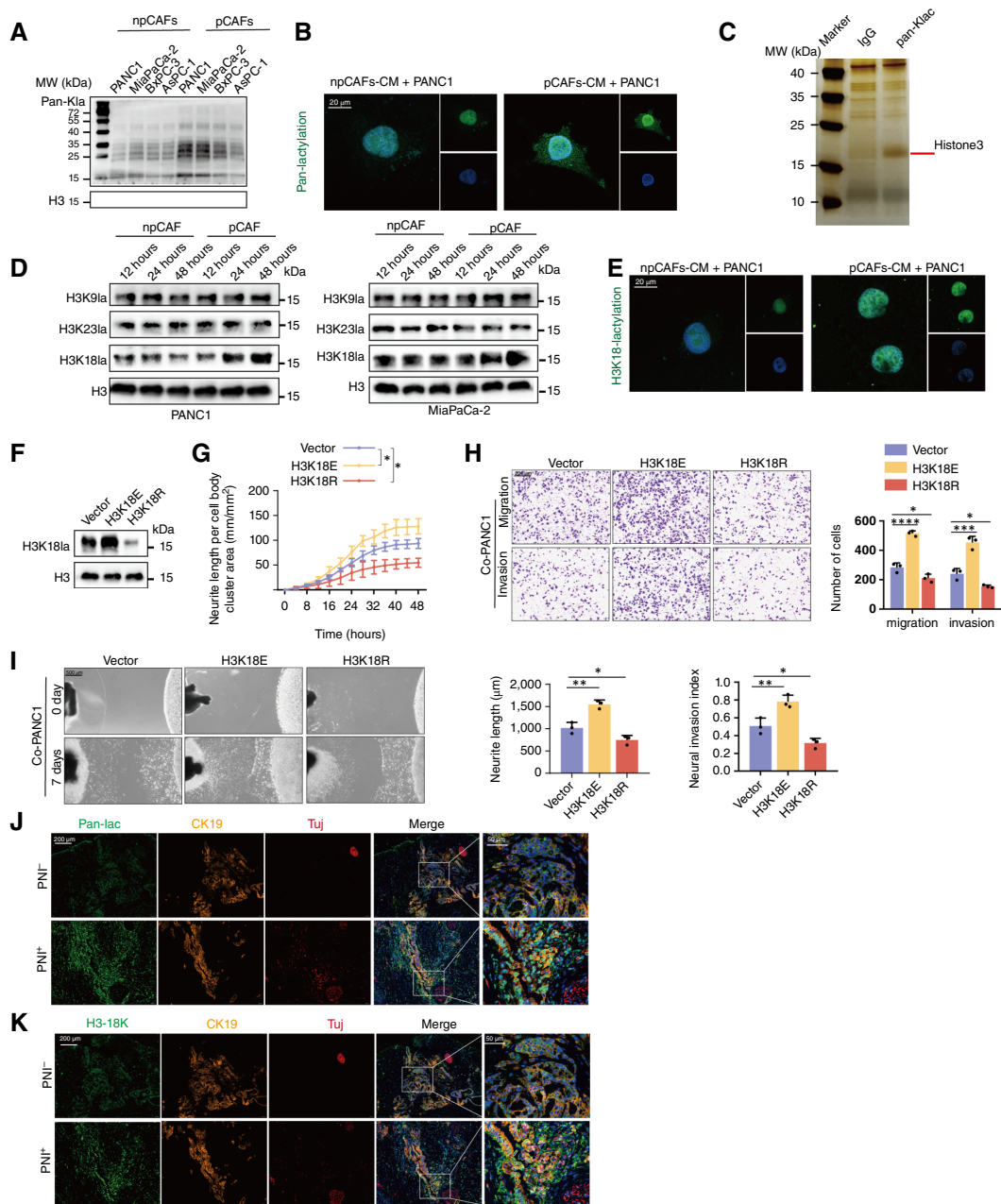


Figure 5.

pCAF-derived lactate regulates PNI through H3K18la. **A–E**, Tumor cells were treated with CM isolated from npCAFs or pCAFs and were used for subsequent experiments. **A**, Western blot of pan-lysine lactylation (Pan-K1a) levels in tumor cells treated as indicated. **B**, Immunofluorescence staining for Pan-K1a in PANC1 cells under the indicated treatments. Scale bar, 20 μm . **C**, Representative silver staining image of lactylation-associated proteins in PANC1 cells treated with pCAFs-CM. The red line highlights the protein bands enriched by the anti-lactylation antibody, which were subsequently analyzed by LC-MS. **D**, Western blot of H3K91a, H3K561a, and H3K181a in tumor cells treated as indicated. **E**, Immunofluorescence staining for H3K18la in tumor cells under the indicated treatments. Scale bar, 20 μm . **F–I**, PANC1 cells transfected with vector, plasmid with H3K18E (lysine to glutamate mutant), or plasmid with H3K18R (lysine to arginine mutant) were used for subsequent experiments. **F**, Western blot of H3K18la in PANC1 cells under the indicated treatments. **G**, Quantitative analysis of neurite length in the Transwell system under the indicated treatments. Phase contrast images of neuronal cells were acquired every 4 hours ($n = 5$ independent experiments; one-way ANOVA test; data are shown as the means \pm SD). **H**, Representative image (left) and quantitative analysis (right) of PANC1 cell migration and invasion in the Transwell system under the indicated treatments. Scale bars, 200 μm . $n = 3$ independent experiments; one-way ANOVA test; data are shown as the means \pm SD. **I**, Neuroinvasive capacity of PANC1 cells following the specified treatment. Scale bars, 500 μm . $n = 3$ independent experiments; one-way ANOVA test; data are shown as the means \pm SD. **J**, mIF staining analysis of pan-lysine lactylation in PNI⁺ and PNI⁻ PDAC tissues. Tuj1 was used as a neuron marker. CK19 was used as a tumor marker. Scale bars, 200 μm . **K**, mIF staining analysis of H3K18la in PNI⁺ and PNI⁻ PDAC tissues. Tuj1 was used as a neuron marker, and CK19 was used as a tumor marker. Scale bars, 200 μm . *, $P < 0.05$; **, $P < 0.01$; ***, $P < 0.001$; ****, $P < 0.0001$.

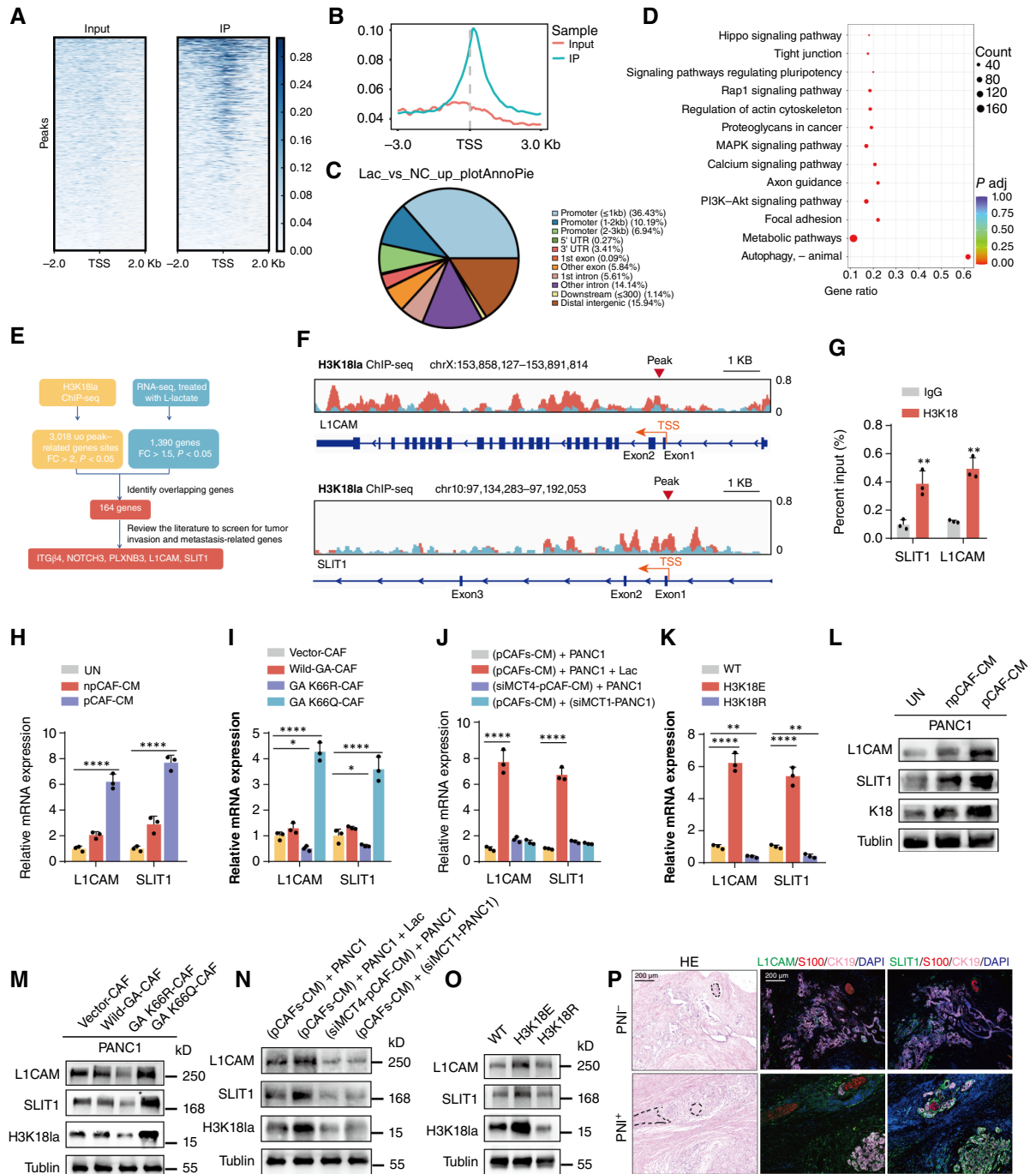


Figure 6.

H3K181a activates L1CAM and SLIT1 transcription in pancreatic cancer. **A** and **B**, Distribution of H3K181a sites relative to the translation start site (TSS). **C**, The pie diagram shows the genomic occupancy of H3K181a binding sites as revealed by ChIP-seq in PANC1 cells. **D**, KEGG analysis of H3K181a peaks. **E**, Bioinformatics analysis filtered L1CAM and SLIT1 as downstream targets of H3K181a. **F**, Integrative Genomics Viewer tracks for *L1CAM* and *SLIT1* from ChIP-seq analysis; peaks are marked with red triangles. **G**, ChIP-qPCR assay of H3K181a status in the *L1CAM* and *SLIT1* genomic region in PANC1 cells ($n = 3$ independent experiments; independent samples t test; data are shown as the means \pm SD). **H-K**, qRT-PCR analysis of *L1CAM* and *SLIT1* mRNA in PANC1 cells and PANC1 cells subjected to specific treatments as described previously ($n = 3$ independent experiments; one-way ANOVA test; data are shown as the means \pm SD). **L-O**, Western blot of L1CAM and SLIT1 in PANC1 cells and PANC1 cells subjected to specific treatments as described previously. **P**, miF staining analysis of L1CAM and SLIT1 in PNI⁺ and PNI⁻ PDAC tissues. S100 was used as a neuron marker, and CK19 was used as a tumor marker. Scale bars, 200 μm . *, $P < 0.05$; **, $P < 0.01$; ****, $P < 0.0001$.

expression (Fig. 6A–C). KEGG pathway analysis of genes associated with H3K18la enrichment demonstrated involvement in signaling pathways crucial for tumor invasion (Fig. 6D). Integrating ChIP-seq data with transcriptomic profiles from RNA-seq of lactate-treated cells, we identified a total of 1,390 genes differentially expressed by at least 1.5-fold in PANC1 cells treated with lactate. Among the 1,390 differentially expressed mRNAs, 164 were enriched in the H3K18la ChIP-seq. *LICAM*, *SLIT1*, *PLXNB3*, *NOTCH3*, and *ITGB* are reportedly involved in neural invasion or metastasis (28–32). qRT-PCR and Western blotting revealed that lactate treatment increased the expression of *LICAM* and *SLIT1* in PANC1 cells without affecting *PLXNB3*, *NOTCH3*, and *ITGB* expression (Fig. 6E; Supplementary Fig. S8C and S8D). *LICAM* and *SLIT1*, known to enhance invasion and metastasis, displayed marked enrichment of H3K18la at their promoter regions (Fig. 6F). ChIP-qPCR assays confirmed elevated levels of H3K18la at *LICAM* and *SLIT1* in lactate-treated PANC1 cells compared with controls (Fig. 6G). Correspondingly, mRNA and protein levels of *LICAM* and *SLIT1* were increased in cells treated with pCAF-derived CM or lactate, and this increase was mitigated by a mutation in *GAPDH* within pCAFs. Moreover, blocking lactate uptake and secretion diminished the pCAF-induced elevation of these genes, akin to the effects observed with the H3K18R lactylation site mutation (Fig. 6H–O). Finally, we assessed *LICAM* and *SLIT1* expression in patient samples with varying degrees of neural invasion and found that both *LICAM* and *SLIT1* were significantly upregulated in patients with severe PNI compared with those without PNI (Fig. 6P). To evaluate the impact of both intrinsic and exogenous lactate on the neuroinvasive capabilities of tumor cells, we knocked down intrinsic lactate production in PANC1 cells using *siLDHA*. qRT-PCR and Western blot assays demonstrated that silencing *LDHA* led to a moderate reduction in the expression of *LICAM* and *SLIT1*. However, this effect was significantly reversed upon the addition of exogenous lactate (Supplementary Fig. S8E and S8F). Collectively, these findings indicate that H3K18la is a key regulator of *LICAM* and *SLIT1* transcription, critically modulating the invasive capabilities of pancreatic cancer cells.

pCAFs enhance PNI of pancreatic cancer via lactate-mediated H3K18la *in vivo*

To evaluate the impact of histone lactylation on pCAF-induced PNI *in vivo*, we developed a sciatic nerve invasion mouse model. We manipulated histone lactylation inhibition by introducing a *GAPDH* mutation in pCAFs and depleting *MCT1* in PANC1 cells. The modified PANC1 cells were treated with CM derived from the indicated pCAFs and injected into the sciatic nerves of BALB/c-nu/nu mice. In xenografts treated with lactic acid, there was an increase in the expression of pan-lactylation, H3K18la, *LICAM*, and *SLIT1* (Fig. 7A). Conversely, introducing a *GAPDH* mutation in pCAFs or depleting *MCT1* in PANC1 cells resulted in decreased levels of pan-lactylation, H3K18la, *LICAM*, and *SLIT1* (Fig. 7A). These changes correspondingly led to a reduction in the severity of PNI and lowered the expression of PNI-associated genes in tumor cells. Treatment with lactic acid led to more severe hind limb paralysis, characterized by a reduction in hind paw width (Fig. 7B).

To better simulate the complex interactions among pCAFs, tumor cells, and nerves *in vivo*, we utilized KPC model mice (*LSL-KRAS^{G12D/+}*, *LSL-TP53^{R172H/+}*, and *PDX-1-CRE^{+/+}*), which spontaneously develop pancreatic cancer. These mice were randomly assigned to four groups and treated with lactic acid, a *GAPDH* inhibitor (heptelidic acid) and an *MCT1* inhibitor (AZD3965). PNI

and tumor innervation were assessed using hematoxylin and eosin staining, mIF, and 3D reconstruction of primary tumor slides of similar size from different groups (Fig. 7C). Exogenous administration of lactate notably enhanced PNI and nerve density compared with the control group and increased the expression of pan-lactylation, H3K18la, *LICAM*, and *SLIT1*. Conversely, inhibiting glycolysis or lactate uptake led to a reduction in PNI and a decrease in intratumoral nerve density. Correspondingly, this inhibition also decreased the expression of pan-lactylation, H3K18la, *LICAM*, and *SLIT1* (Fig. 7C–E). These findings collectively indicate that pCAFs promote PNI in pancreatic cancer through lactate-driven H3K18la *in vivo*.

Pan-lac/H3K18la is associated with PNI and poor prognosis in patients with PDAC

To evaluate the clinical implications of our discoveries in PDAC, we analyzed the expression of pan-lac, H3K18la, *LICAM*, and *SLIT1* in 152 tissue samples from patients with PDAC using mIF staining (Fig. 8A). We observed that increased staining for pan-lac and H3K18la was associated with greater PNI and elevated expression of *LICAM* and *SLIT1* (Fig. 8B–E). Additionally, severe PNI correlated with higher concentrations of lactic acid (Fig. 8F). Kaplan–Meier survival analysis demonstrated that elevated H3K18la expression in tissues was linked to reduced overall survival and DFS (Fig. 8G–J). Similarly, elevated tissue levels of *LICAM* and *SLIT1* were associated with poorer patient prognosis (Fig. 8K–N). Collectively, our study reveals that pCAFs promote pancreatic cancer PNI by shaping a high-lactate TME, upregulating tumor cell histone H3K18la, and transcriptionally activating the expression of genes associated with neural infiltration (Fig. 8O).

Discussion

In patients with pancreatic cancer, PNI is a critical factor that is strongly associated with a poor prognosis, increased pain, and decreased life expectancy. The underlying mechanisms of PNI are complex, involving intricate interactions among various signaling pathways and molecules. Despite the considerable progress made in understanding PNI, the precise mechanisms of PNI, particularly about how the TME mediates its progression, remain poorly understood. Our study elucidates that CAFs derived from patients with PDAC with positive PNI significantly enhance tumor cell invasion toward nerves. This is due to increased acetylation levels of the glycolytic enzyme *GAPDH* in CAFs, boosting glycolysis and lactate secretion, which leads to the lactylation of histone H3K18 on tumor cells; transcriptionally activating *LICAM* and *SLIT1*; and ultimately promoting PNI. Our research highlights the innovative value of CAF-derived lactate in the TME, promoting PNI in pancreatic cancer through histone H3K18la in tumor cells. These insights have important clinical implications, offering new avenues for the development of effective therapies to combat PNI and improve outcomes in patients with pancreatic cancer.

Despite the fact that mitochondrial metabolism is the most efficient pathway for ATP generation, proliferating cells such as cancer cells and CAFs prefer the glycolytic pathways with lactate produced, termed “the Warburg effect” and “the reverse Warburg effect” (33, 34). The activation of CAFs is frequently associated with glycolysis activation induced by TGF β -related signaling pathways (35). Tumor-derived TGF β has been widely recognized as a key regulator of myCAF differentiation. Previous studies have demonstrated that TGF β promotes the transition of fibroblasts into myCAFs by

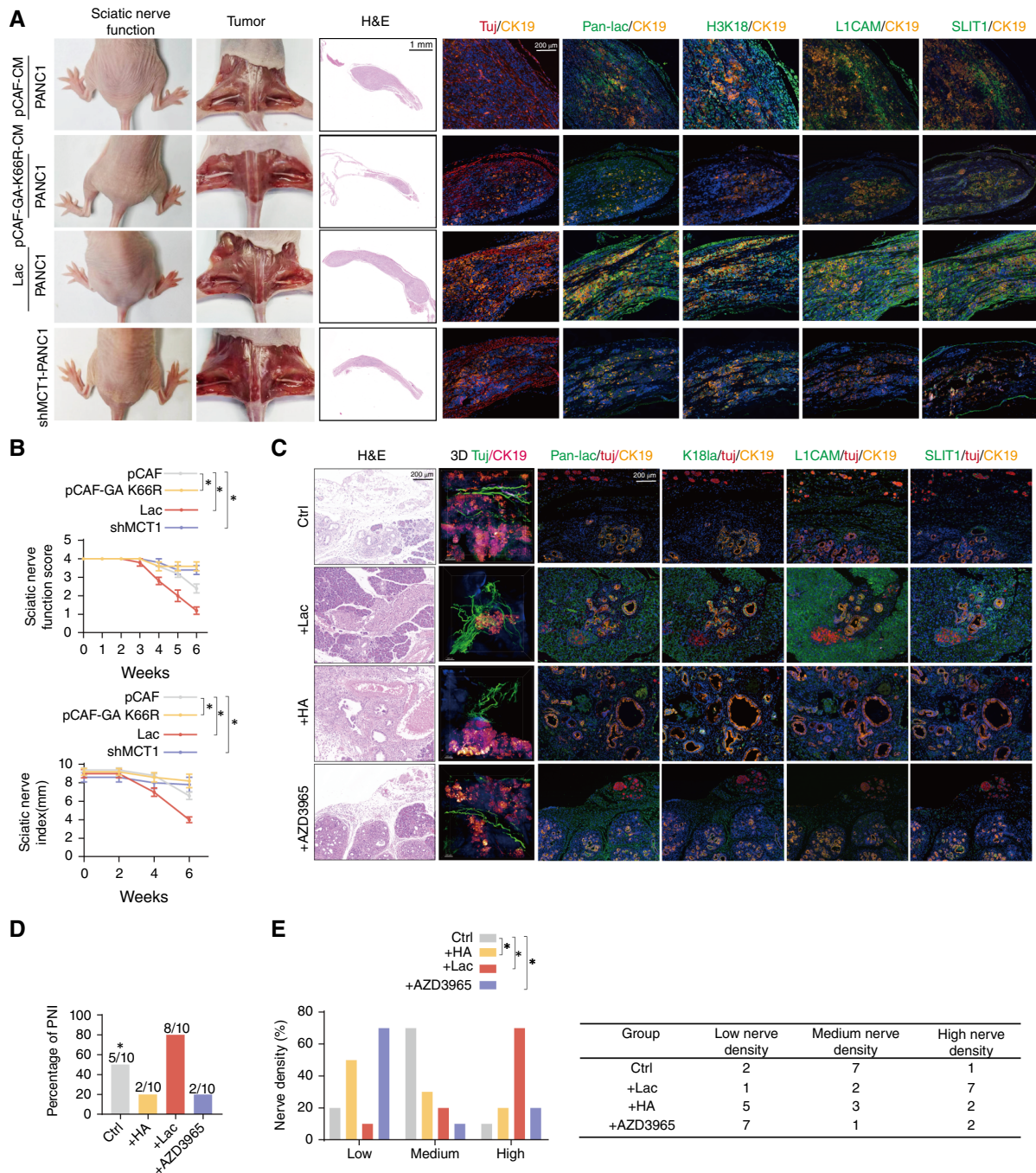


Figure 7.

pCAFs enhance PNI of pancreatic cancer via lactate-mediated H3K18la *in vivo*. **A**, Gross and surgical images, hematoxylin and eosin (H&E) staining, and mIF images. mIF showed pan-lac, H3K18, LICAM, and SLIT1 expression in the sciatic nerve invasion model. The dotted line indicates the tumor boundary. Tuj1 served as a neuronal marker, and CK19 was used as a tumor marker. H&E, scale bars, 1,000 μ m. mIF, scale bars, 200 μ m. **B**, Sciatic nerve function scores and sciatic nerve indexes of mice treated as indicated ($n = 5$ mice per group). Kruskal-Wallis test with Dunn multiple comparisons test; data are shown as the means \pm SD. **C-E**, KPC mice (*LSL-KRAS*^{G12D/+}; *LSL-TRP53*^{R172H/+}; *PDX-1-CRE*^{+/+}) were divided into four groups, with three groups respectively receiving i.p. injections of sodium lactate (1 g/kg), oral administration of the MCT1 inhibitor AZD3965 (100 mg/kg), and i.p. injections of heptenoic acid (1 mg/kg). $n = 10$ mice per group. **C**, Representative hematoxylin and eosin staining. mIF and 3D reconstruction images showing PNI status and pan-lac, H3K18, LICAM, and SLIT1 expression in KPC mice treated as indicated. Tuj1 served as a neuron marker. CK19 was used as a tumor marker. Hematoxylin and eosin and mIF, scale bars, 200 μ m. 3D scale bars, 500 μ m. **D**, Proportion of PNI in KPC mice under the specified treatments ($n = 10$ mice per group). Fisher exact test. **E**, Nerve density percentage (left) and number (right) in KPC mice following the indicated treatments ($n = 10$ mice per group; χ^2 test). *, $P < 0.05$. HA, heptenoic acid.

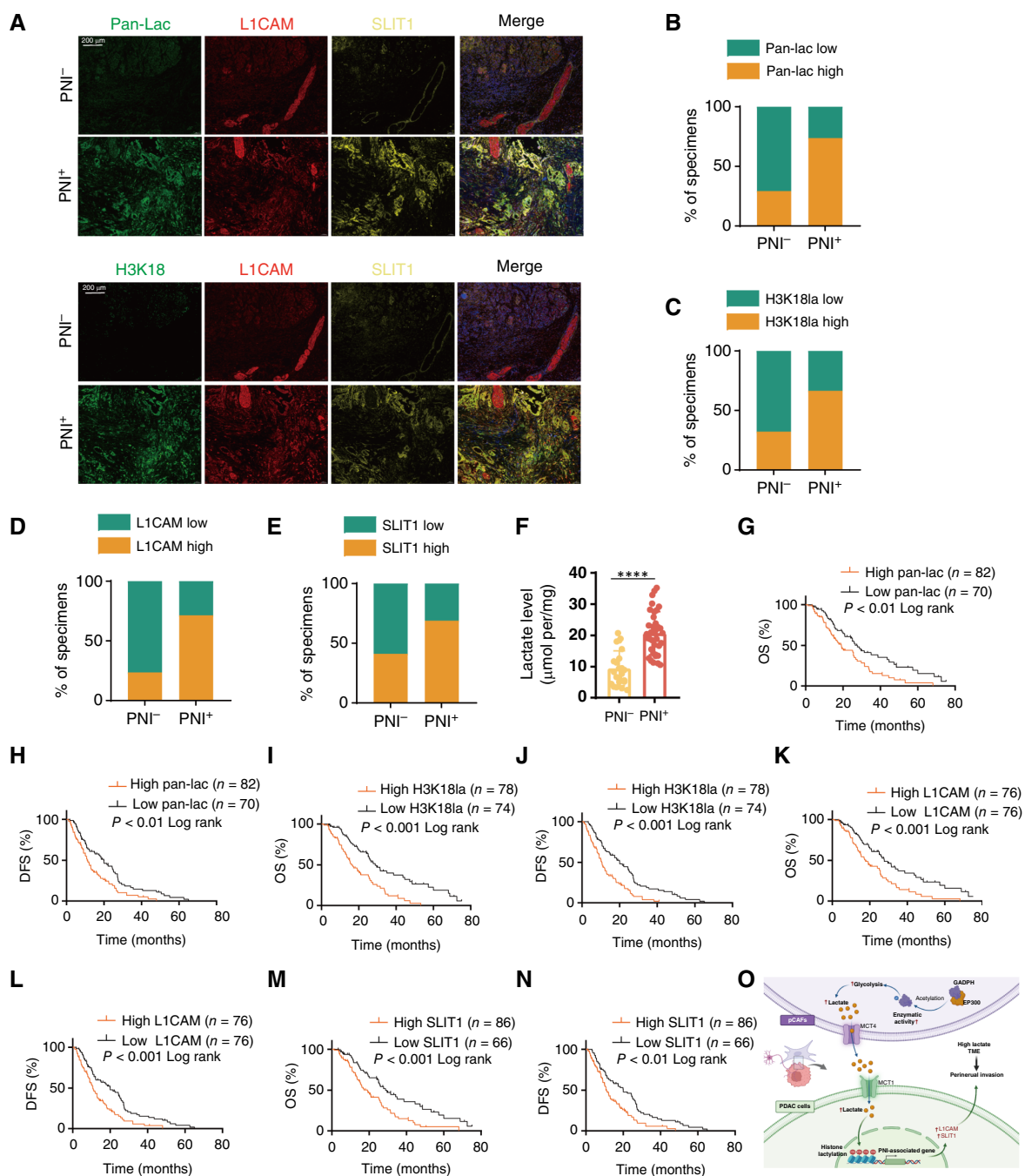


Figure 8.

Pan-lac/H3K1818a is associated with PNI and poor prognosis in patients with PDAC. **A**, mIF results for pan-lac, H3K1818, L1CAM, and SLIT1 expression in patients with PDAC (n = 152). Scale bars, 200 μm. **B–E**, Quantitative breakdown of the specimen percentages featuring low or high expression of pan-lac (**B**), H3K1818 (**C**), L1CAM (**D**), and SLIT1 (**E**) across PNI⁻ and PNI⁺ groups. **F**, Lactate levels of PNI⁻ and PNI⁺ tissues. **G–N**, Kaplan–Meier analysis of overall survival (OS) and DFS of patients with PDAC categorized by high or low pan-lac expression (**G** and **H**), high or low H3K1818 expression (**I** and **J**), high or low L1CAM expression (**K** and **L**), and high or low SLIT1 expression (**M** and **N**). **O**, Schematic illustration delineating the mechanism by which pCAFs promote pancreatic cancer PNI by shaping a high-lactate TME, upregulating tumor cell histone H3K1818a and transcriptionally activating the expression of genes associated with neural infiltration. Data are presented as mean ± SD. ****, P < 0.0001. **O**, Created with BioRender.com. Hu, C. (2025) <https://BioRender.com/h04t962>.

enhancing ECM production, activating EGFR/ERBB2 signaling, and antagonizing inflammatory CAF phenotypes, thereby shaping the tumor stroma to facilitate tumor progression (36–38). These

findings align with our observation of elevated TGFβ levels in PNI⁺ pancreatic cancer tissues, which likely contribute to the enrichment of myCAFs in the pCAF population. In addition to promoting

myCAF differentiation, TGF β also plays a critical role in driving glycolytic activation in CAFs. Studies have shown that TGF β induces metabolic reprogramming by downregulating IDH3a, stabilizing HIF1 α , and enhancing glycolysis, thereby supporting reciprocal tumor–CAF interactions and sustaining protumorigenic activity (39, 40). Furthermore, TGF β stimulates the activation of the mTOR/AKT signaling pathway in CAFs, as demonstrated by both transcriptomic and protein-level analyses. This activation leads to the phosphorylation of P300, which enhances its enzymatic activity and promotes the acetylation of GAPDH. Previous research has reported that TGF β can activate the mTOR/AKT pathway (41, 42) and that AKT-mediated phosphorylation enhances P300 enzymatic activity (43, 44). This sequence of events establishes a feedback loop that sustains the metabolic reprogramming of pCAFs, contributing to their proinvasive behavior. This novel understanding of the molecular cross-talk in the TME underscores the potential for targeting TGF β signaling and associated metabolic pathways as therapeutic strategies to limit tumor progression in pancreatic cancer. Hui and colleagues (45) demonstrated that circulating lactate serves as a key carbon source for the tricarboxylic acid cycle in tumor cells, highlighting the pivotal role of exogenous lactate in supporting tumor metabolism and growth. In the pancreatic cancer microenvironment, CAFs are often more abundant than tumor cells, highlighting their critical role in shaping the metabolic landscape. Our findings suggest that CAF-derived lactate exerts a more pronounced effect on metabolic and epigenetic reprogramming compared with tumor cell–intrinsic lactate. This aligns with findings in prostate cancer, in which stromal lactate has been shown to drive lipid droplet accumulation and histone modifications, ultimately enhancing tumor aggressiveness (14). These insights emphasize the contribution of exogenous lactate from CAFs in promoting PNI in pancreatic cancer, further underscoring the therapeutic potential of targeting stromal-tumor metabolic cross-talk. Interestingly, although gene set enrichment analysis revealed significant activation of the glycolytic pathway in pCAFs, we did not observe corresponding differences in the mRNA levels of key glycolytic enzymes. This suggests that glycolytic activation in pCAFs may be predominantly driven by posttranscriptional or posttranslational modifications, such as enzyme acetylation or enhanced enzymatic activity, rather than transcriptional regulation. These findings underscore the complexity of glycolytic regulation and the need for complementary methods to fully elucidate pathway dynamics.

Current research underscores the substantial heterogeneity and plasticity of CAFs, revealing distinct subpopulations with unique roles in pancreatic cancer progression (46). The identified subgroups include myCAFs and iCAFs (36, 37), and more recently identified subpopulations include antigen-presenting CAFs (apCAF; ref. 47), CD105⁺ and CD105[−] CAFs, LRRCL15⁺ CAFs (48), Gli1⁺ CAFs, and Hoxb6⁺ CAFs (49), among others, and each subtype has a distinct influence on tumor dynamics (46). In soft-tissue sarcomas, glycolytic CAFs share similar transcriptional profiles with myCAFs and rely on glycolysis to impede cytotoxic T-cell infiltration into the tumor parenchyma via the Cxcl16/Cxcr6 axis (50). Through single-cell analysis of PDAC, Wang and colleagues (51) identified a novel fibroblast subtype—metabolic CAF (meCAF)—characterized by a highly activated metabolic state and enhanced glycolysis, which is linked to poor prognosis but improved response to immunotherapy. Additionally, the study suggests that myCAFs have the potential to convert into meCAFs, aligning with previous research indicating that CAFs exhibit high plasticity and can transition between different states (37, 52). Our study specifically

focused on CAFs related to PNI in PDAC. By analyzing single-cell data from human PDAC samples obtained from other studies (20, 21), we discovered a significant increase in the proportion of CAFs in PNI-positive pancreatic cancer samples compared with PNI-negative samples (PNI⁺ vs. PNI[−]: 13.8% vs. 5.6%). Notably, myCAFs were more prevalent among the CAF subtypes. Further pathway enrichment analysis revealed that myCAFs were significantly enriched in the glycolytic pathway, and the proportion of myCAFs was significantly correlated with the severity of PNI, suggesting that myCAFs play a major role in shaping the high-lactate microenvironment that promotes PNI in pancreatic cancer. Our study highlights the heterogeneity of CAFs in the pancreatic cancer microenvironment and suggests, based on scRNA-seq, the potential presence of a glycolysis-enriched myCAF subset within the pCAF population that may shape the TME to facilitate PNI. However, our study has limitations in definitively identifying specific markers and functional mechanisms of these subpopulations. Future research will focus on the isolation and detailed characterization of these clusters to elucidate their precise roles and explore their potential as therapeutic targets.

The GAPDH enzyme is essential for the aerobic breakdown of glucose and is often overexpressed in various human cancers, in which it is linked to reduced patient survival (53–55). Although the GAPDH gene produces a single mRNA and protein without alternative splicing, growing evidence indicates that GAPDH has diverse roles in various cellular processes (56). The flux of GAPDH has been shown to be the rate-limiting step that separates upstream and downstream glycolytic processes (57). Glycolytic flux is most sensitive to changes in GAPDH activity when the intermediate metabolite distribution is uneven, highlighting the importance of GAPDH regulation for controlling glycolysis in the microenvironment and suggesting potential regulatory strategies (57). GAPDH acetylation, an evolutionarily conserved mechanism, regulates its activity by varying with the carbon source, as observed in *Salmonella typhimurium*, thereby modulating its catalytic function accordingly (58, 59). High glucose levels stimulate K254 acetylation, enhancing GAPDH activity and promoting cell proliferation and tumor formation, whereas nuclear GAPDH acetylation at lysine 160 by p300/CREB-binding protein (CBP) further enhances the acetylation and activity of P300/CBP and mediates apoptosis (22, 60). In this study, we found that p300-mediated acetylation of K66 enhances GAPDH's catalytic activity and promotes a high-lactate metabolic microenvironment. Notably, the conservation of Lys-66 across species suggests its essential role in regulating activity and highlights its potential for preclinical targeted research and translational applications.

Histone posttranslational modifications are essential for regulating gene expression, as they create docking sites for chromatin modulators, which in turn influence numerous biological processes (61, 62). As a key epigenetic modification, H3K18la reflects the metabolic state of the cell and influences cellular behavior and fate by regulating gene expression patterns (63). Li and colleagues (64) demonstrated that the transcription factor Glis1 promotes somatic cell reprogramming into pluripotent stem cells by regulating glycolysis-driven H3K18la and H3K27Ac modifications, highlighting the interplay between metabolism and epigenetics in cell fate determination. In drug-resistant microenvironments, lactate-driven histone lactylation under hypoxia promotes colorectal cancer progression and bevacizumab resistance, whereas in the tumor immune microenvironment, PERK-driven glucose metabolism in monocyte-derived macrophages facilitates immunosuppression in glioblastoma

through histone lactylation, underscoring its role as a crucial regulatory mechanism in both tumor progression and immune evasion (18, 65). Li and colleagues (66) identified a crucial positive feedback loop involving glycolysis, H3K18la, and TTK/BUB1B that accelerates PDAC progression through lactate-mediated histone modifications. Our research found that tumor cells in patients with a higher degree of PNI exhibit more pronounced histone lactylation, with MCT4 in CAFs and MCT1 in tumor cells being crucial for lactate transport, which elucidates for the first time the key mechanism of metabolic and epigenetic coupling in the tumor-neural invasion microenvironment. Further research is needed to determine whether histone lactylation in tumor cells primarily depends on lactate derived from the microenvironment and if targeting lactate transport between different cell types could effectively inhibit pancreatic cancer metastasis. In pulmonary fibrosis, communication between alveolar epithelial cells and myofibroblasts, mediated by lactylation, especially through H3K18la's regulation of YTHDF1, is vital for the development of arsenite-induced idiopathic pulmonary fibrosis (67). In the TME, TIMP1 acts as a key mediator of lactate-driven histone lactylation in CAFs, highlighting its significance in driving the advancement and spread of clear-cell renal cell carcinoma (68). Our findings reveal that H3K18la is a key regulator of *L1CAM* and *SLIT1* transcription, highlighting the unique role of lactylation as a metabolic modification in the precise regulation of PNI and underscoring its potential as a target for therapeutic intervention.

In summary, our study provides novel insights into the regulatory mechanisms of PNI in pancreatic cancer. We demonstrated that the expression of PNI-associated factors is controlled by an epigenetic mechanism involving histone lactylation, driven by the high-lactate microenvironment created by pCAFs. Our findings enhance the understanding of the role of epigenetic modifications in PNI and shed light on the intercellular communication within the TME that underlies this

process. Furthermore, our study suggests that targeting lactate transport in the TME and inhibiting histone lactylation in cancer cells may be promising therapeutic strategies to prevent PNI in pancreatic cancer.

Authors' Disclosures

No disclosures were reported.

Authors' Contributions

T. Li: Validation, visualization, methodology, writing—original draft. C. Hu: Validation. T. Huang: Validation. Y. Zhou: Validation. Q. Tian: Validation. H. Chen: Validation. R. He: Validation. Y. Yuan: Investigation. Y. Jiang: Investigation. H. Jiang: Validation. K. Huang: Validation. D. Cheng: Writing—original draft. R. Chen: Supervision, funding acquisition. S. Zheng: Supervision, funding acquisition.

Acknowledgments

This study was supported by grants from the National Natural Science Foundation of China (grant numbers 82372859 to S. Zheng, 82072639 and 82372858 to R. Chen, 82203691 to C. Hu, and 82403081 to H. Chen); the Natural Science Foundation of Guangdong Province (grant number 2024A1515013216 to C. Hu); the Special Fund of the “Dengfeng Plan” of Guangdong Provincial People's Hospital, China (grant numbers KJ012019509 and DFJH2020027 to R. Chen); the National Key Clinical Specialty Construction Project (2021–2024, grant number 2022YW030009 to R. Chen); and the Guangzhou Science and Technology Plan Project (grant numbers 2025A04J4765 to S. Zheng and 202201010944 to K. Huang).

Note

Supplementary data for this article are available at Cancer Research Online (<http://cancerres.aacrjournals.org/>).

Received August 31, 2024; revised February 4, 2025; accepted March 21, 2025; posted first March 26, 2025.

References

- Winkler F, Venkatesh HS, Amit M, Batchelor T, Demir IE, Deneen B, et al. Cancer neuroscience: state of the field, emerging directions. *Cell* 2023;186:1689–707.
- Bapat A A, Hostetter G, Von Hoff DD, Han H. Perineural invasion and associated pain in pancreatic cancer. *Nat Rev Cancer* 2011;11:695–707.
- Demir IE, Boldis A, Pfiztinger P L, Teller S, Brunner E, Klose N, et al. Investigation of Schwann cells at neoplastic cell sites before the onset of cancer invasion. *J Natl Cancer Inst* 2014;106:dju184.
- Sinha S, Fu Y-Y, Grimont A, Ketcham M, Lafaro K, Saglimbeni J A, et al. PanIN neuroendocrine cells promote tumorigenesis via neuronal cross-talk. *Cancer Res* 2017;77:1868–79.
- Lin Q, Zheng S, Yu X, Chen M, Zhou Y, Zhou Q, et al. Standard pancreatoduodenectomy versus extended pancreatoduodenectomy with modified retroperitoneal nerve resection in patients with pancreatic head cancer: a multicenter randomized controlled trial. *Cancer Commun (Lond)* 2023;43:257–75.
- Jurcak N, Zheng L. Signaling in the microenvironment of pancreatic cancer: transmitting along the nerve. *Pharmacol Ther* 2019;200:126–34.
- Xu W, Liu J, Zhang J, Lu J, Guo J. Tumor microenvironment crosstalk between tumors and the nervous system in pancreatic cancer: molecular mechanisms and clinical perspectives. *Biochim Biophys Acta Rev Cancer* 2024;1879:189032.
- Bressy C, Lac S, Nigri J, Leca J, Roques J, Lavaut M-N, et al. LIF drives neural remodeling in pancreatic cancer and offers a new candidate biomarker. *Cancer Res* 2018;78:909–21.
- Zheng S, Hu C, Lin Q, Li T, Li G, Tian Q, et al. Extracellular vesicle-packaged PIAT from cancer-associated fibroblasts drives neural remodeling by mediating m5C modification in pancreatic cancer mouse models. *Sci Transl Med* 2024;16:ead0178.
- Banh RS, Biancur DE, Yamamoto K, Sohn ASW, Walters B, Kuljanin M, et al. Neurons release serine to support mRNA translation in pancreatic cancer. *Cell* 2020;183:1202–18.e25.
- Auciello FR, Bulusu V, Oon C, Tait-Mulder J, Berry M, Bhattacharyya S, et al. A stromal lysolipid-autotaxin signaling axis promotes pancreatic tumor progression. *Cancer Discov* 2019;9:617–27.
- Kumagai S, Koyama S, Itahashi K, Tanegashima T, Lin Y-T, Togashi Y, et al. Lactic acid promotes PD-1 expression in regulatory T cells in highly glycolytic tumor microenvironments. *Cancer Cell* 2022;40:201–18.e9.
- Chen J, Zhu Y, Wu C, Shi J. Engineering lactate-modulating nanomedicines for cancer therapy. *Chem Soc Rev* 2023;52:973–1000.
- Ippolito L, Comito G, Parri M, Iozzo M, Duatti A, Virgilio F, et al. Lactate rewires lipid metabolism and sustains a metabolic-epigenetic axis in prostate cancer. *Cancer Res* 2022;82:1267–82.
- Pavlova NN, Zhu J, Thompson CB. The hallmarks of cancer metabolism: still emerging. *Cell Metab* 2022;34:355–77.
- Li X, Yang Y, Zhang B, Lin X, Fu X, An Y, et al. Lactate metabolism in human health and disease. *Signal Transduct Target Ther* 2022;7:305.
- Liberti MV, Locasale JW. Histone lactylation: a new role for glucose metabolism. *Trends Biochem Sci* 2020;45:179–82.
- De Leo A, Ugolini A, Yu X, Scirocchi F, Scocozza D, Peixoto B, et al. Glucose-driven histone lactylation promotes the immunosuppressive activity of monocyte-derived macrophages in glioblastoma. *Immunity* 2024;57:1105–23.e8.
- Wang X, Liu X, Xiao R, Fang Y, Zhou F, Gu M, et al. Histone lactylation dynamics: unlocking the triad of metabolism, epigenetics, and immune regulation in metastatic cascade of pancreatic cancer. *Cancer Lett* 2024;598:217117.
- Steele NG, Carpenter ES, Kemp SB, Sirihorachai VR, The S, Delrosario L, et al. Multimodal mapping of the tumor and peripheral blood immune landscape in human pancreatic cancer. *Nat Cancer* 2020;1:1097–112.
- Peng J, Sun B-F, Chen C-Y, Zhou J-Y, Chen Y-S, Chen H, et al. Single-cell RNA-seq highlights intra-tumoral heterogeneity and malignant progression in pancreatic ductal adenocarcinoma. *Cell Res* 2019;29:725–38.

22. Li T, Liu M, Feng X, Wang Z, Das I, Xu Y, et al. Glyceraldehyde-3-phosphate dehydrogenase is activated by lysine 254 acetylation in response to glucose signal. *J Biol Chem* 2014;289:3775–85.
23. Bond ST, Howlett KF, Kowalski GM, Mason S, Connor T, Cooper A, et al. Lysine post-translational modification of glyceraldehyde-3-phosphate dehydrogenase regulates hepatic and systemic metabolism. *FASEB J* 2017;31:2592–602.
24. Huang W-C, Chen C-C. Akt phosphorylation of p300 at Ser-1834 is essential for its histone acetyltransferase and transcriptional activity. *Mol Cell Biol* 2005;25:6592–602.
25. Tang Q, Markby GR, MacNair AJ, Tang K, Tkacz M, Parys M, et al. TGF- β -induced PI3K/AKT/mTOR pathway controls myofibroblast differentiation and secretory phenotype of valvular interstitial cells through the modulation of cellular senescence in a naturally occurring in vitro canine model of myxomatous mitral valve disease. *Cell Prolif* 2023;56:e13435.
26. Tasdogan A, Faubert B, Ramesh V, Ubellacker JM, Shen B, Solmonson A, et al. Metabolic heterogeneity confers differences in melanoma metastatic potential. *Nature* 2020;577:115–20.
27. Richiandone E, Al Roumi R, Lardinois F, Giolito MV, Ambroise J, Boidot R, et al. MCT1-dependent lactate recycling is a metabolic vulnerability in colorectal cancer cells upon acquired resistance to anti-EGFR targeted therapy. *Cancer Lett* 2024;598:217091.
28. Na'ara S, Amit M, Gil Z. L1CAM induces perineural invasion of pancreas cancer cells by upregulation of metalloproteinase expression. *Oncogene* 2019;38:596–608.
29. Chen D-L, Zeng Z-L, Yang J, Ren C, Wang D-S, Wu W-J, et al. L1cam promotes tumor progression and metastasis and is an independent unfavorable prognostic factor in gastric cancer. *J Hematol Oncol* 2013;6:43.
30. Amodio V, A D, Betts J, Bartesaghi S, Zhang Y, Richard-Londt A, et al. A PML/slit axis controls physiological cell migration and cancer invasion in the CNS. *Cell Rep* 2017;20:411–26.
31. Zuo Q, Yang Y, Lyu Y, Yang C, Chen C, Salman S, et al. Plexin-B3 expression stimulates MET signaling, breast cancer stem cell specification, and lung metastasis. *Cell Rep* 2023;42:112164.
32. Ruan S, Lin M, Zhu Y, Lum L, Thakur A, Jin R, et al. Integrin β 4-targeted cancer immunotherapies inhibit tumor growth and decrease metastasis. *Cancer Res* 2020;80:771–83.
33. Pavlides S, Whitaker-Menezes D, Castello-Cros R, Flomenberg N, Witkiewicz AK, Frank PG, et al. The reverse Warburg effect: aerobic glycolysis in cancer associated fibroblasts and the tumor stroma. *Cell Cycle* 2009;8:3984–4001.
34. Yan W, Wu X, Zhou W, Fong M Y, Cao M, Liu J, et al. Cancer-cell-secreted exosomal miR-105 promotes tumour growth through the MYC-dependent metabolic reprogramming of stromal cells. *Nat Cell Biol* 2018;20:597–609.
35. Wang Y, Wang X, Bai B, Shaha A, He X, He Y, et al. Targeting Src SH3 domain-mediated glycolysis of HSC suppresses transcriptome, myofibroblastic activation, and colorectal liver metastasis. *Hepatology* 2024;80:578–94.
36. Öhlund D, Handly-Santana A, Biffi G, Elyada E, Almeida AS, Ponz-Sarvise M, et al. Distinct populations of inflammatory fibroblasts and myofibroblasts in pancreatic cancer. *J Exp Med* 2017;214:579–96.
37. Biffi G, Oni TE, Spielman B, Hao Y, Elyada E, Park Y, et al. IL1-Induced JAK/STAT signaling is antagonized by TGF β to shape CAF heterogeneity in pancreatic ductal adenocarcinoma. *Cancer Discov* 2019;9:282–301.
38. Mucciolo G, Araos Henriquez J, Jihad M, Pinto Teles S, Manansala JS, Li W, et al. EGFR-activated myofibroblasts promote metastasis of pancreatic cancer. *Cancer Cell* 2024;42:101–18.e111.
39. Zhang D, Wang Y, Shi Z, Liu J, Sun P, Hou X, et al. Metabolic reprogramming of cancer-associated fibroblasts by IDH3 α downregulation. *Cell Rep* 2015;10:1335–48.
40. Li Q, Zhu C-C, Ni B, Zhang Z-Z, Jiang S-H, Hu L-P, et al. Lysyl oxidase promotes liver metastasis of gastric cancer via facilitating the reciprocal interactions between tumor cells and cancer associated fibroblasts. *EBioMedicine* 2019;49:157–71.
41. Shi Q, Huang F, Wang Y, Liu H, Deng H, Chen Y-G. HER2 phosphorylation induced by TGF-beta promotes mammary morphogenesis and breast cancer progression. *J Cell Biol* 2024;223:e202307138.
42. Guillén Díaz-Maroto N, Sanz-Pamplona R, Berdiel-Acer M, Cimas FJ, García E, Gonçalves-Ribeiro S, et al. Noncanonical TGF β pathway relieves the blockade of IL1 β /TGF β -mediated crosstalk between tumor and stroma: TGFBR1 and TAK1 inhibition in colorectal cancer. *Clin Cancer Res* 2019;25:4466–79.
43. Liu Y, Denlinger CE, Rundall BK, Smith PW, Jones DR. Suberoylanilide hydroxamic acid induces Akt-mediated phosphorylation of p300, which promotes acetylation and transcriptional activation of RelA/p65. *J Biol Chem* 2006;281:31359–68.
44. Serra C, Palacios D, Mozzetta C, Forcales S V, Morante I, Ripani M, et al. Functional interdependence at the chromatin level between the MKK6/p38 and IGF1/PI3K/AKT pathways during muscle differentiation. *Mol Cell* 2007;28:200–13.
45. Hui S, Ghergurovich JM, Morscher RJ, Jang C, Teng X, Lu W, et al. Glucose feeds the TCA cycle via circulating lactate. *Nature* 2017;551:115–8.
46. Halbrook CJ, Lyssiotis CA, Pasca di Magliano M, Maitra A. Pancreatic cancer: advances and challenges. *Cell* 2023;186:1729–54.
47. Elyada E, Bolisetty M, Laise P, Flynn WF, Courtois ET, Burkhart RA, et al. Cross-species single-cell analysis of pancreatic ductal adenocarcinoma reveals antigen-presenting cancer-associated fibroblasts. *Cancer Discov* 2019;9:1102–23.
48. Dominguez CX, Müller S, Keerthivasan S, Koeppen H, Hung J, Gierke S, et al. Single-cell RNA sequencing reveals stromal evolution into LRRC15⁺ myofibroblasts as a determinant of patient response to cancer immunotherapy. *Cancer Discov* 2020;10:232–53.
49. Garcia PE, Adoumie M, Kim EC, Zhang Y, Scales MK, El-Tawil YS, et al. Differential contribution of pancreatic fibroblast subsets to the pancreatic cancer stroma. *Cell Mol Gastroenterol Hepatol* 2020;10:581–99.
50. Broz MT, Ko EY, Ishaya K, Xiao J, De Simone M, Hoi XP, et al. Metabolic targeting of cancer associated fibroblasts overcomes T-cell exclusion and chemoresistance in soft-tissue sarcomas. *Nat Commun* 2024;15:2498.
51. Wang Y, Liang Y, Xu H, Zhang X, Mao T, Cui J, et al. Single-cell analysis of pancreatic ductal adenocarcinoma identifies a novel fibroblast subtype associated with poor prognosis but better immunotherapy response. *Cell Discov* 2021;7:36.
52. Sahai E, Atsaturov I, Cukierman E, DeNardo DG, Egeblad M, Evans RM, et al. A framework for advancing our understanding of cancer-associated fibroblasts. *Nat Rev Cancer* 2020;20:174–86.
53. Liu S, Sun Y, Jiang M, Li Y, Tian Y, Xue W, et al. Glyceraldehyde-3-phosphate dehydrogenase promotes liver tumorigenesis by modulating phosphoglycerate dehydrogenase. *Hepatology* 2017;66:631–45.
54. Strausberg RL, Greenhut SF, Grouse LH, Schaefer CF, Buetow KH. In silico analysis of cancer through the Cancer Genome Anatomy Project. *Trends Cell Biol* 2001;11:S66–71.
55. Révillon F, Pawlowski V, Hornez L, Peyrat JP. Glyceraldehyde-3-phosphate dehydrogenase gene expression in human breast cancer. *Eur J Cancer* 2000;36:1038–42.
56. Meyer-Siegler K, Mauro DJ, Seal G, Wurzer J, deRiel JK, Sirover MA. A human nuclear uracil DNA glycosylase is the 37-kDa subunit of glyceraldehyde-3-phosphate dehydrogenase. *Proc Natl Acad Sci U S A* 1991;88:8460–4.
57. Shestov AA, Liu X, Ser Z, Cluntun AA, Hung YP, Huang L, et al. Quantitative determinants of aerobic glycolysis identify flux through the enzyme GAPDH as a limiting step. *Elife* 2014;3:e03342.
58. Balmer ML, Ma EH, Bantug GR, Grählert J, Pfister., Glatter T, et al. Memory CD8⁺ T cells require increased concentrations of acetate induced by stress for optimal function. *Immunity* 2016;44:1312–24.
59. Guan K-L, Xiong Y. Regulation of intermediary metabolism by protein acetylation. *Trends Biochem Sci* 2011;36:108–16.
60. Sen N, Hara MR, Kornberg MD, Cascio MB, Bae B-I, Shahani N, et al. Nitric oxide-induced nuclear GAPDH activates p300/CBP and mediates apoptosis. *Nat Cell Biol* 2008;10:866–73.
61. Yang J, Xu J, Wang W, Zhang B, Yu X, Shi S. Epigenetic regulation in the tumor microenvironment: molecular mechanisms and therapeutic targets. *Signal Transduct Target Ther* 2023;8:210.
62. Morgan MAJ, Shilatifard A. Epigenetic moonlighting: catalytic-independent functions of histone modifiers in regulating transcription. *Sci Adv* 2023;9:eadg6593.
63. Hu X, Huang X, Yang Y, Sun Y, Zhao Y, Zhang Z, et al. Dux activates metabolism-lactylation-MET network during early iPSC reprogramming with Brg1 as the histone lactylation reader. *Nucleic Acids Res* 2024;52:5529–48.
64. Li L, Chen K, Wang T, Wu Y, Xing G, Chen M, et al. Glis1 facilitates induction of pluripotency via an epigenome-metabolome-epigenome signalling cascade. *Nat Metab* 2020;2:882–92.
65. Li W, Zhou C, Yu L, Hou Z, Liu H, Kong L, et al. Tumor-derived lactate promotes resistance to bevacizumab treatment by facilitating autophagy enhancer protein RUBCNL expression through histone H3 lysine 18 lactylation (H3K18la) in colorectal cancer. *Autophagy* 2024;20:114–30.
66. Li F, Si W, Xia L, Yin D, Wei T, Tao M, et al. Positive feedback regulation between glycolysis and histone lactylation drives oncogenesis in pancreatic ductal adenocarcinoma. *Mol Cancer* 2024;23:90.
67. Wang P, Xie D, Xiao T, Cheng C, Wang D, Sun J, et al. H3K18 lactylation promotes the progression of arsenite-related idiopathic pulmonary fibrosis via YTHDF1/m6A/NREP. *J Hazard Mater* 2024;461:132582.
68. Kong W, He J, Zhou Q, Zhou X, Wei X, Yang Y, et al. Histone lactylation-related genes correlate with the molecular patterns and functions of cancer-associated fibroblasts and have significant clinical implications in clear cell renal cell carcinoma. *Heliyon* 2024;10:e33554.